JGR Solid Earth

RESEARCH ARTICLE

Key Points:
- We use convection models with plate motion history to constrain the mantle viscosity, both its relative variations and absolute values
- Strong plates and weak plate margins with non-uniform viscosity are critical in reproducing the geoid and surface plate motion
- The lower mantle viscosity is ~1.3–2.5 × 10^{22} Pa·s and ~30 and ~600–1,000 times higher than that in the transition zone and asthenosphere

Supporting Information:
Supporting Information may be found in the online version of this article.

Correspondence to:
W. Mao and S. Zhong,
wei.mao@colorado.edu;
shijie.zhong@colorado.edu

Constraints on Mantle Viscosity From Intermediate-Wavelength Geoid Anomalies in Mantle Convection Models With Plate Motion History

Wei Mao[1] and **Shijie Zhong[1]**

[1]Department of Physics, University of Colorado, Boulder, CO, USA

Abstract The Earth's long- and intermediate-wavelength geoid anomalies are surface expressions of mantle convection and are sensitive to mantle viscosity. While previous studies of the geoid provide important constraints on the mantle radial viscosity variations, the mantle buoyancy in these studies, as derived from either seismic tomography or slab density models, may suffer significant uncertainties. In this study, we formulate 3-D spherical mantle convection models with plate motion history since the Cretaceous that generate dynamically self-consistent mantle thermal and buoyancy structures, and for the first time, use the dynamically generated slab structures and the observed geoid to place important constraints on the mantle viscosity. We found that non-uniform weak plate margins and strong plate interiors are critical in reproducing the observed geoid and surface plate motion, especially the net lithosphere rotation (i.e., degree-1 toroidal plate motion). In the best-fit model, which leads to correlation of 0.61 between the modeled and observed geoid at degrees 4–12, the lower mantle viscosity is ~1.3–2.5 × 10^{22} Pa·s and is ~30 and ~600–1,000 times higher than that in the transition zone and asthenosphere, respectively. Slab structures and the geoid are also strongly affected by slab strength, and the observations prefer moderately strong slabs that are ~10–100 times stronger than the ambient mantle. Finally, a thin weak layer below the 670-km phase change on a regional scale only in subduction zones produces stagnant slabs in the mantle transition zone as effectively as a weak layer on a global scale.

1. Introduction

Mantle viscosity is a key to understanding fundamental Earth science questions including the large-scale mantle convection and Earth's dynamic evolution and also important societally relevant questions such as global sea-level change. While significant progresses have been made to determine the mantle viscosity through the studies of laboratory-based deformation experiments (e.g., Karato, 2008), glacial isostatic adjustment (e.g., Mitrovica & Forte, 2004; Peltier, 1998), geoid (e.g., Hager, 1984; Hager & Richards, 1989; Ricard et al., 1993), and post-seismic relaxation (e.g., Pollitz et al., 2001), mantle viscosity remains poorly constrained.

The Earth's long wavelength geoid anomalies are dynamic expressions of mantle convection and are controlled by mantle buoyancy and viscosity structure (e.g., Hager et al., 1985; Hager & Richards, 1989; King, 1995; Ricard et al., 1993). Most previous geoid studies have derived mantle density anomalies (i.e., the buoyancy) from seismic tomography models (e.g., Ghosh et al., 2010; Spasojevic et al., 2010; Hager & Richards, 1989; Liu & Zhong, 2016; Rudolph et al., 2015; Yang & Gurnis, 2016). However, it remains a challenge on how to convert seismic anomalies into mantle buoyancy, due to uncertainties in seismic structure and mantle thermodynamic parameters (e.g., Karato & Karki, 2001; Simmons et al., 2009; Stixrude & Lithgow-Bertelloni, 2011, 2005). Another method of deriving mantle buoyancy is to use subduction history to empirically estimate slab structures and hence density anomalies in the mantle (e.g., Hager, 1984; Lithgow-Bertelloni & Richards, 1998; Ricard et al., 1993). However, the mantle flow and buoyancy structures are strongly affected by the temperature- and depth-dependent viscosity (e.g., Zhong et al., 2000). Therefore, it is unclear whether the inverted viscosity structures are dynamically consistent with the buoyancy structures derived as a *priori* in the geoid modeling.

Most geoid studies have only considered 1-D radial viscosity variations in instantaneous flow models. However, mantle viscosity is strongly temperature-dependent, which leads to lateral viscosity variations (LVV). LVV could have strong effect on the geoid, especially at the subduction zones (e.g., Moresi & Gurnis, 1996;

Tosi, Čadek, & Martinec, 2009; Zhong & Davies, 1999; Čadek & Fleitout, 2003). However, there have been debates on how strong the LVV is, especially for slabs (Billen & Hirth, 2007; Hines & Billen, 2012). While laboratory experiments for the deformation of olivine and numerical models of subduction illustrate that slab viscosity could be 10^4 to 10^5 times larger than the ambient mantle (i.e., 10^{24}–10^{25} Pa·s) (e.g., Billen & Hirth, 2007; Karato, 2008), geoid studies indicate that slab is only moderately strong and has similar viscosity as the ambient mantle (Moresi & Gurnis, 1996; Yang & Gurnis, 2016; Zhong & Davies, 1999). Furthermore, the effects of LVV are also dependent on the buoyancy structure that is used (Zhong & Davies, 1999). For example, Ghosh et al. (2010) found that LVV could strongly affect geoid calculated from slab density models but not for those from seismic models (Moucha et al., 2007).

Mantle convection models with plate motion history have successfully reproduced mantle structures observed in seismic tomography models (e.g., Bunge et al., 1998; McNamara & Zhong, 2005; Steinberger et al., 2012), particularly the degree-2 lower mantle structures or African and Pacific large low shear velocity provinces (LLSVPs; McNamara & Zhong, 2005; Zhang et al., 2010; Bower et al., 2013) and subducted slab structures including the horizontally deflected slab structures in the western Pacific (Mao & Zhong, 2018, 2019; referred to as MZ18, MZ19 hereafter). Recently, by conducting quantitative comparisons between this type of convection models and seismic models, MZ19 found significant correlations between these models at long- and intermediate-wavelengths, especially above 1,000 km depth for spherical harmonic degrees up to 20. Therefore, using the dynamically generated mantle buoyancy structures and by fitting the observed geoid, these mantle convection models could provide more robust and self-consistent constraints on mantle viscosity. In this study, we formulate 3-D spherical mantle convection models with plate motion history (Seton et al., 2012) to constrain the mantle viscosity by comparing results of convection models with seismic models, observed geoid and surface plate motion. Because our time-dependent convection models are computationally expensive, our goal here is to seek for the most robust general features in mantle viscosity, rather than for viscosity inversion. The paper is organized as follows. In the next section we will describe the mantle convection model setup. We will then present results of our convection models and comparisons with different observations. Finally, we will present discussions and conclusions.

2. Methods and Model Setup

2.1. Governing Equations

We use the 3-D spherical shell geometry mantle convection code CitcomS to solve conservation equations of the mass, momentum and energy with the Boussinesq approximation and infinitely large Prandtl number. The dimensionless conservation equations are (Zhong et al., 2000, 2008):

$$\nabla \cdot \vec{u} = 0, \tag{1}$$

$$-\nabla P + \nabla \cdot \left(\eta \dot{\varepsilon} \right) + \left[RaT - \sum_j Rb^j \Gamma_j \right] \hat{e}_r = 0, \tag{2}$$

$$\frac{\partial T}{\partial t} + \left(\vec{u} \cdot \nabla \right) T = \nabla^2 T + H, \tag{3}$$

where $\vec{u}$ is the velocity vector, P is the dynamic pressure, η is the viscosity, $\dot{\varepsilon}$ is the strain rate tensor, T is temperature, Γ_j is a phase change function for the j-th phase change if multiple changes exist in the model, Ra and Rb^j are the thermal Rayleigh number and phase change Rayleigh number, respectively, $\hat{e}_r$ is the unit vector in radial direction, t is the time, and H is the internal heat generation rate.

Ra and Rb^j are defined as:

$$Ra = \frac{\rho g \alpha \Delta T R^3}{\kappa \eta_0}, \tag{4}$$

$$Rb^j = \frac{\Delta\rho_j g R^3}{\kappa\eta_0}, \tag{5}$$

where ρ is the mantle reference density, g is the gravitational acceleration, α is the thermal expansivity, ΔT is the temperature difference between the surface and CMB, κ is the thermal diffusivity, η_0 is the reference viscosity, $\Delta\rho_j$ is the density jump for the j-th phase change, and R is the radius of the Earth.

The internal heat generation rate H is defined as

$$H = \frac{QR^2}{\rho C_p \kappa \Delta T}, \tag{6}$$

where Q is the volumetric heat production rate and C_p is the specific heat. In this study, we fix H to be 100 and the corresponding Q is 7.7×10^{-12} W/kg for reference parameters used here.

2.2. Phase Change and Viscosity Structure

A phase change function formulation is used here to represent phase changes (Christensen & Yuen, 1985; Zhong & Gurnis, 1994). The phase change function is defined in dimensionless form as

$$\Gamma_j = \frac{1}{2}\left[1 + \tanh\left(\frac{\pi_j}{\delta_j}\right)\right], \tag{7}$$

where π_j is the dimensionless "excess pressure" defined as

$$\pi_j = d - d_j - \gamma_j\left(T - T_j\right), \tag{8}$$

where d is the depth, d_j, δ_j, and T_j are the reference depth, phase transition width and temperature of phase change j, and γ_j is the Clapeyron slope. γ_j is normalized by $\rho g R/\Delta T$, d, d_j, and δ_j are normalized by Earth Radius R.

In this study, we only consider the spinel to post-spinel phase change at ∼670 km depth and we fix the Clapeyron slope to be −2.0 MPa/K (dimensionless value of −0.024) that is consistent with mineral physics studies (e.g., Fei et al., 2004; Litasov et al., 2005). Most cases in this study consider the superplasticity effect due to the phase change (Karato, 2008; Panasyuk & Hager, 1998; Solomatov & Reese, 2008) by including either a global or regional weak layer below the phase change boundary, as this weak layer plays an important role in producing horizontally deflected slabs in the transition zone (MZ18 and MZ19). This weak layer is defined using the phase function Γ. When $\Gamma < 0.5$, the mantle viscosity is the same as that in the transition zone. However, for $0.5 < \Gamma < 0.99$, the mantle is considered in superplastic post-spinel phase, and its viscosity pre-factor is reduced to be 10 times smaller than that in the transition zone. The effective thickness of viscosity reduction due to this weak layer is ∼60 km. The weak layer may only occur in regions with large radial flow velocity (Panasyuk & Hager, 1998; Solomatov & Reese, 2008), that is, downwelling regions. Therefore, we also consider the weak layer that occurs on a regional scale using the temperature criteria

$$\delta T = T - T_{ave} < -0.01, \tag{9}$$

where δT and T_{ave} are the non-dimensional temperature anomaly and horizontally averaged temperature, respectively.

Mantle viscosity in our models is both depth- and temperature-dependent and the non-dimensional form is

$$\eta(T,r) = \eta_r(r)\exp\left[E\left(0.5 - T\right)\right], \tag{10}$$

where $\eta_r(r)$ is the depth-dependent pre-factor and E is the non-dimensional activation energy. The mantle is divided into four layers with different $\eta_r(r)$: the lithosphere (0–130 km depth); the asthenosphere

Table 1
Model Parameters

Parameters	Value
Earth's radius, R	6,370 km
Mantle thickness, h	2,870 km
Mantle density, ρ	3,300 kg/m^3
Gravitational acceleration, g	9.8 m/s^2
Thermal expansivity, α[a]	3×10^{-5}/K
Reference temperature difference, ΔT	2500 K
Thermal diffusivity, κ[a]	10^{-6} m^2/s
Gas constant, R_{gas}	8.314 J/(K mol)
Specific heat, C_p	1,250 J/(kg K)
Spinel to post-spinel density change, $\Delta\rho_1/\rho$	8%
Spinel to post-spinel phase change width, δ_1	40 km
Spinel to post-spinel phase change reference depth, d_1	670 km
Spinel to post-spinel phase change reference temperature, T_1	1,573 K
Spinel to post-spinel Clapeyron slope, γ_1	−2.0 MPa/K
Heat production rate, Q	7.7×10^{-12} W/kg
Reference viscosity, η_0[b]	1.3×10^{22} Pa·s

[a]Thermal expansivity decreases by a factor of 2.5 from surface to the CMB, while thermal diffusivity increases by a factor of 2.18 from surface to the CMB. [b]The reference viscosity depends on the Rayleigh number Ra, here we only present the value at $Ra = 5 \times 10^7$.

(130–300 km depth); the mantle transition zone (300–670 km depth); and the lower mantle (670–2,870 km depth). In the models where the asthenosphere and mantle transition zone have the same viscosity pre-factor, these two layers are treated as a single layer (i.e., the upper mantle; 130–670 km depth). The lithosphere viscosity pre-factor η_{Lith} and the lower mantle viscosity pre-factor η_{LM} are fixed at 1 and 2, respectively. The viscosity pre-factor ratio between the lower mantle and the asthenosphere $\omega = \eta_{LM} / \eta_{Asth}$ (or between the lower mantle and the upper mantle η_{LM} / η_{UM}) and between the lower mantle and the mantle transition zone $\beta = \eta_{LM} / \eta_{TZ}$ are varied in our models. The non-dimensional activation energy E is mostly 9.21 (i.e., corresponding to dimensional value of 191 KJ/mol if parameters in Table 1 are used) that results in a total viscosity contrast V_E of 10^4 which corresponds to the total temperature difference of 2500 K in the mantle. Because the largest temperature contrast in our slab only model is only ~1300 K, the total viscosity contrast due to temperature is 10^2 and the lithosphere viscosity varies from 10^{22} to 10^{24} Pa·s. E is also varied in some models to test the effect of different slab viscosity.

2.3. Initial and Boundary Conditions

We use time-dependent plate motions (Seton et al., 2012) as surface velocity boundary conditions, while the CMB is free-slip, similar to previous studies (e.g., Bunge et al., 1998; McNamara & Zhong, 2005). The surface dimensionless temperature is prescribed as a constant 0 (i.e., 0°C), while the CMB has a thermally insulating boundary condition as in MZ18. The insulating CMB prevents thermal upwelling plumes from being generated so that our models can concentrate on the contribution of subducted slabs. The insulating CMB boundary condition may be justified given that our models only cover relatively short geological time periods (65–200 Myr).

The initial mantle temperature below the lithosphere is 0.52 (or 1300°C) everywhere. For most cases, the initial temperature in oceanic lithosphere is calculated from a plate model (Turcotte & Schubert, 2014) based on lithospheric ages (Müller et al., 2013) at the beginning of model calculations. The initial non-dimensional

temperature for continental lithosphere increases linearly from 0 at the surface to 0.52 at 130 km depth. Most of our model calculations are initiated at 130 Ma using plate motion history from Seton et al. (2012) and the initial ages of oceanic lithosphere at 130 Ma are from Müller et al. (2013).

Our calculations are performed on parallel computers Cheyenne and RMACC Summit which are operated by the National Center for Atmospheric Research and University of Colorado at Boulder, respectively. We use a mesh with $12 \times 128 \times 128 \times 80$ grid points and employ grid refinements near the surface, the phase transition, and the CMB in the radial direction. With this grid, the models have a horizontal resolution of 50 km at the surface and 30 km near the CMB.

2.4. Geoid Calculation

We compute the present-day geoid anomalies caused by mantle thermal (i.e., buoyancy) structure for each model. In computing the geoid, we replace the present-day surface velocity (i.e., plate motion) boundary condition with a free-slip boundary condition because prescribing plate motions may introduce artifacts in the computed buoyancy induced dynamic topography (e.g., Davies, 1988). Additionally, we reduce viscosity for plate margins in the otherwise high viscosity lithosphere such that the surface plate motions can be predicted and compared with the observed (e.g., Ghosh et al., 2010; Zhong & Davies, 1999) and more details can be seen in Sections 3.6 and 4.2.

The model geoid anomalies include contributions from dynamic topography at the surface and CMB and interior density anomalies including those due to phase change topography caused by convective thermal structures. Calculations of the geoid consider the effect of self-gravitation and are done in a spherical harmonic domain (Zhong et al., 2008).

To compare the observed and model geoid anomalies, we compute the correlation and variance reduction using the spherical harmonic coefficients of the observed geoid $\{a_{lm}, b_{lm}\}$ and model geoid $\{c_{lm}, d_{lm}\}$ (Becker & Boschi, 2002; Liu & Zhong, 2016). The degree-correlation at degree l is

$$C_l = \frac{\sum_{m=0}^{l}\left(a_{lm}c_{lm} + b_{lm}d_{lm}\right)}{\sqrt{\sum_{m=0}^{l}\left(a_{lm}^2 + b_{lm}^2\right)}\sqrt{\sum_{m=0}^{l}\left(c_{lm}^2 + d_{lm}^2\right)}}. \tag{11}$$

The total correlation from degrees l_{min} to l_{max} is

$$C_{l_{min}-l_{max}} = \frac{\sum_{l=l_{min}}^{l_{max}}\sum_{m=0}^{l}\left(a_{lm}c_{lm} + b_{lm}d_{lm}\right)}{\sqrt{\sum_{l=l_{min}}^{l_{max}}\sum_{m=0}^{l}\left(a_{lm}^2 + b_{lm}^2\right)}\sqrt{\sum_{l=l_{min}}^{l_{max}}\sum_{m=0}^{l}\left(c_{lm}^2 + d_{lm}^2\right)}}. \tag{12}$$

The variance reduction from degrees l_{min} to l_{max} is

$$V_{l_{min}-l_{max}} = 1 - \frac{\sum_{l=l_{min}}^{l_{max}}\sum_{m=0}^{l}\left[\left(a_{lm} - c_{lm}\right)^2 + \left(b_{lm} - d_{lm}\right)^2\right]}{\sum_{l=l_{min}}^{l_{max}}\sum_{m=0}^{l}\left(a_{lm}^2 + b_{lm}^2\right)}. \tag{13}$$

The geoid power at degree l is

$$P_l = \sqrt{\sum_{m=0}^{l}\left(a_{lm}^2 + b_{lm}^2\right)}. \tag{14}$$

3. Results

In this section, we present results of mantle convection models with prescribed surface plate motion and compare the model results of the present-day mantle structure, plate motion and geoid with the observed. In total, 31 time-dependent cases are computed (Table 2) to explore the effects of different model parameters, particularly the mantle viscosity structure.

Table 2
Input Parameters and Geoid Correlations and Variance Reductions for Different Models[a]

Case	ω	β	Ra	$Time$ (Myr)	E	$C_{2\text{-}12}$	$V_{2\text{-}12}$	$C_{4\text{-}12}$	$V_{4\text{-}12}$
A1	100	100	5e7	130	9.21	0.73	0.34	0.45	0.20
A2	10	10	5e7	130	9.21	0.20	−0.49	−0.54	−3.53
A3	30	30	5e7	130	9.21	0.35	0.11	−0.32	−0.79
A4	60	60	5e7	130	9.21	0.55	0.30	0.11	−0.26
A5	200	200	5e7	130	9.21	0.39	0.14	0.33	0.09
A6	300	300	5e7	130	9.21	0.09	−0.07	0.34	0.06
A7[b]	100	100	5e7	130	9.21	0.32	0.10	0.08	−0.24
B1	100	30	5e7	130	9.21	0.38	0.14	0.00	−0.17
B2	200	30	5e7	130	9.21	0.55	0.23	0.29	0.09
B3	300	30	5e7	130	9.21	0.58	0.31	0.46	0.21
B4	600	30	5e7	130	9.21	0.56	0.30	0.61	0.37
B5	1,000	30	5e7	130	9.21	0.52	0.24	0.61	0.37
B5e[c]	1,000	30	5e7	130	9.21	0.51	0.26	0.48	0.21
B5f[c]	1,000	30	5e7	130	9.21	0.60	0.28	0.61	0.30
B6[d]	2,000	30	5e7	130	9.21	0.40	0.14	0.53	0.28
B7[d]	3,000	30	5e7	130	9.21	0.39	0.15	0.56	0.31
B8	1,000	10	5e7	130	9.21	0.47	0.21	0.51	0.26
B9	1,000	60	5e7	130	9.21	0.27	0.07	0.54	0.29
B10	1,000	100	5e7	130	9.21	0.17	0.02	0.53	0.27
C1	10	100	5e7	130	9.21	0.25	−0.17	−0.56	−2.65
C2	30	100	5e7	130	9.21	0.44	0.19	−0.37	−0.78
C3	60	100	5e7	130	9.21	0.55	0.24	−0.09	−0.22
C4	10	300	5e7	130	9.21	0.16	−0.13	−0.54	−2.30
C5	30	300	5e7	130	9.21	0.36	0.13	−0.36	−0.79
C6	60	300	5e7	130	9.21	0.55	0.23	−0.10	−0.31
D1	1,000	30	2.5e7	130	9.21	0.31	0.07	0.51	0.25
D2	1,000	30	1e8	130	9.21	0.57	0.28	0.62	0.38
D3	1,000	30	2e8	130	9.21	0.50	0.23	0.58	0.34
E1	1,000	30	5e7	130	0	0.52	0.27	0.50	0.25
E2	1,000	30	5e7	130	4.21	0.56	0.30	0.53	0.28
E3	1,000	30	5e7	130	13.82	0.22	0.05	0.50	0.25
F1	1,000	30	5e7	65	9.21	0.36	0.13	0.65	0.42
F2	1,000	30	5e7	200	9.21	0.59	0.28	0.51	0.26

[a]ω, β, Ra, $Time$, E, $C_{2\text{-}12}$, $V_{2\text{-}12}$, $C_{4\text{-}12}$, and $V_{4\text{-}12}$ represent viscosity ratio between the lower and upper mantles (or the asthenosphere), viscosity ratio between the lower mantle and the transition zone, Rayleigh number, model total running time (in Myr), activation energy, correlations, and variance reductions between the modeled geoid and observed geoid at degrees 2–12 and 4–12, respectively. [b]Case A7 has a global weak layer beneath the spinel-to-post-spinel phase transition, while all the other models have a regional weak layer in which the weak layer only exists at regions near slabs. [c]Case B5e and B5f are models modified from Case B5 with a uniformly weak D″ layer and with low viscosity only for the cold slabs in the D″ layer, respectively. [d]In Cases B6 and B7, the viscosity of slabs in the asthenosphere are increased by 10 times to maintain coherent slab structures.
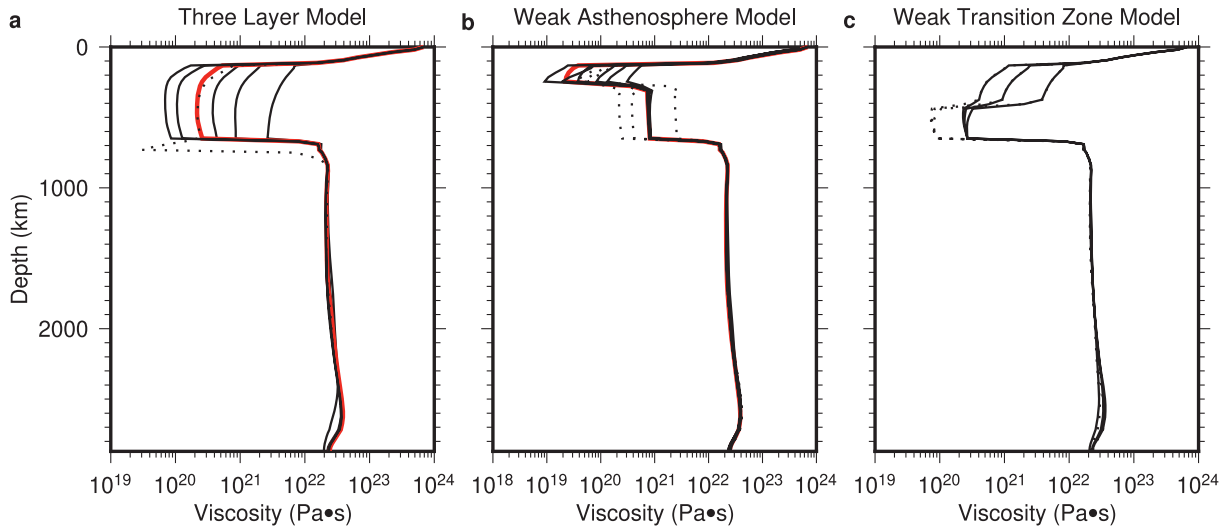
Figure 1. Viscosity profiles for different groups of models. (a) Three layer models: Cases A1–A7. Red solid, black solid, and black dotted lines are for Cases A1, A2–A6, and A7, respectively. (b) Four layer models with a weak asthenosphere. Red solid and black dashed lines are for Cases B5 and B8–B10, respectively. Black solid lines are for Cases B1–B4 and B6–B7. (c) Four layer models with a weak mantle transition zone. Black solid and dashed lines are for Cases C1–C3 and C4–C6, respectively. Note that this is not the simple $\eta_r(r)$ profile but the horizontally averaged viscosity profile.

3.1. Three Layer Models

In this section, we present three layer models (Figure 1a) in which the mantle is divided into three viscosity layers: the lithosphere (0–130 km), the upper mantle (130–670 km) and the lower mantle (670–2,870 km) that have different viscosity pre-factors (Equation 10). We first present Case A1 in which the viscosity pre-factor ratio between the lower mantle and upper mantle, $\omega = \eta_{LM} / \eta_{UM}$, is 100 (Table 2). This case starts at 130 Ma. This case is nearly identical to the standard case in MZ18 except that the global weak layer beneath the spinel-to-post-spinel phase transition in MZ18 is replaced with a regional weak layer that only exists in regions with subducted slabs based on criterion defined by Equation 9 (Figure S1a). Similar to MZ18, Case A1 reproduces well the slab structures observed in seismic models (e.g., SEMUCB-WM1 [French & Romanowicz, 2014, 2015; Figure S2]), such as the stagnant slabs in the western Pacific (Figures 2a–2e), the slabs in the lower mantle in the circum-Pacific and Tethys subduction zones (Figures 2b, 2c, and 2f–2h). This suggests that a regional weak layer beneath the phase change works equally well to reproduce the stagnant slab structures in some of the subduction zones as a global weak layer in MZ18.

Figures 3a–3d shows the observed geoid and the modeled geoid of Cases A1. It is well known that the geoid highs at degrees 4–12 are mostly located at subduction zones (e.g., Hager, 1984), such as circum-Pacific subduction zones and Tethys subduction zones (Figure 3a). Our modeled geoid shows a similar pattern as the observed geoid at degrees 4–12 (Figure 3c). The correlation between the observed geoid and the modeled geoid of Cases A1 at degrees 4–12, C_{4-12}, is 0.45, and the variance reduction, V_{4-12}, is 0.20 (Figure 4a). The correlations are highest at degrees 4 and 5, and decrease with increasing spherical harmonic degree l (Figure 5a). The modeled geoid power also decreases with increasing l as the observed (Figure 5a).

If the long-wavelengths ($l = 2$–3) geoid anomalies are included, the observed geoid highs are mostly centered in the Pacific and Africa, above the LLSVPs (Figure 3b). However, the amplitude of the model geoid highs in these two regions and the geoid power at degrees 2–3 for Case A1 are significantly lower than the observed (Figures 3d and 5a). The total correlations C_{2-12} and variance reductions V_{2-12} between Case A1 and the observed geoid are 0.73 and 0.34 (Figure 4b). We suggest that the relatively small power of the model geoid at degrees 2–3 from Case A1 be partially due to the lack of upwelling thermal structure in the lower mantle in our models with a thermally insulating CMB. Even with only downwelling structures, the lower mantle thermal structures in our models correlate well with the seismic structure at degrees 2–3 with correlation higher than 0.8 (MZ19). However, upwelling thermal structure in the lower mantle contributes
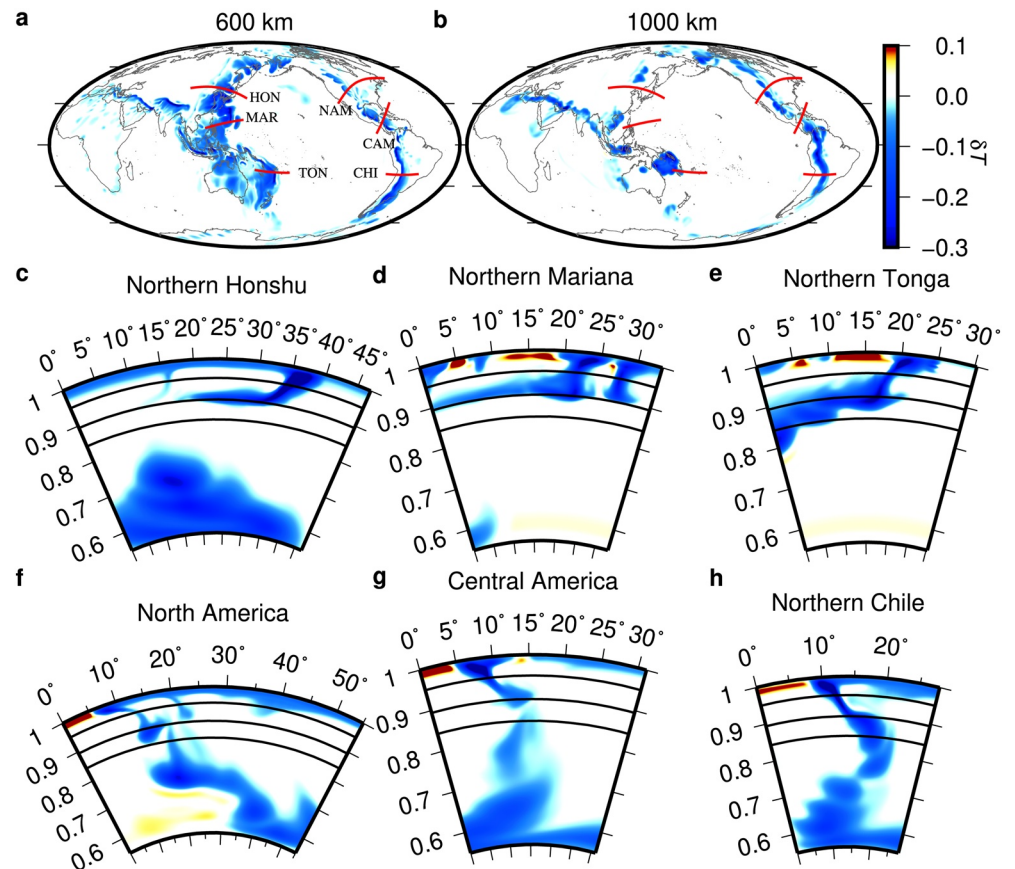
Figure 2. Present-day dimensionless temperature anomalies (δT) of Case A1. Panels (a)–(b) are map view of temperature anomalies at 600 and 1,000 km depths, respectively. Panels (c)–(h) are cross-sectional view of temperature anomalies in the northern Honshu, northern Mariana, northern Tonga, North America, Central America, and northern Chile subduction zones, respectively. These six cross-sections are marked as red lines in panels (a) and (b) and annotated as HON, MAR, TON, NAM, CAM, and CHI, respectively. The three thick black lines in panels (c)–(h) correspond to 410, 670, and 1,000 km depths, respectively.

significantly to the overall power at degrees 2–3 (e.g., MZ19) that could affect the long wavelength geoid significantly (e.g., Hager & Richards, 1989; Ricard et al., 1993).

To test the contribution of upwelling structures including LLSVPs to the geoid, we replace the buoyancy structure below 1,500 km in Case A1 by that converted from seismic velocity anomalies of SEMUCB-WM1 (French & Romanowicz, 2014, 2015) using the conversion factor $\wedge = \dfrac{\partial V_s / V_s}{\partial \rho / \rho} = 3.4$ (Liu & Zhong, 2016).

While the correlation of the recomputed geoid to the observed remains similar (Figures 4 and 5), the recomputed geoid power at degree 2 improves significantly (Figure 5a), suggesting that upwelling thermal structures including LLSVP structures in the lower mantle may contribute significantly to the degree 2–3 geoid. However, the geoid at degrees 4–12 is largely controlled by the structure in the top 1,500 km of the mantle which is dominated by cold slabs (e.g., MZ19).

Cases A2–A6 differ from Case A1 only in that the viscosity ratio between the upper and lower mantles, ω, is changed from 100 to 10, 30, 60, 200, and 300, respectively (Table 2). Similar to Case A1, these cases are computed for 130 Myr. Note here that we change the ratio by varying the upper mantle viscosity while fixing the lower mantle viscosity. Compared with Case A1, Cases A2–A4 with a larger upper mantle viscosity show significantly thicker slabs (e.g., Case A2 in Figures S3a–S3d), while Cases A5–A6 with a smaller viscosity in the upper mantle show thinner slabs in the upper mantle (e.g., Case A6 in Figures S3e–S3h). Note that for too weak upper mantle, some slabs cannot maintain a continuous structure in the upper mantle (Figures S3e and S3h for the Northern Honshu and North America slabs). The geoid correlations and variance
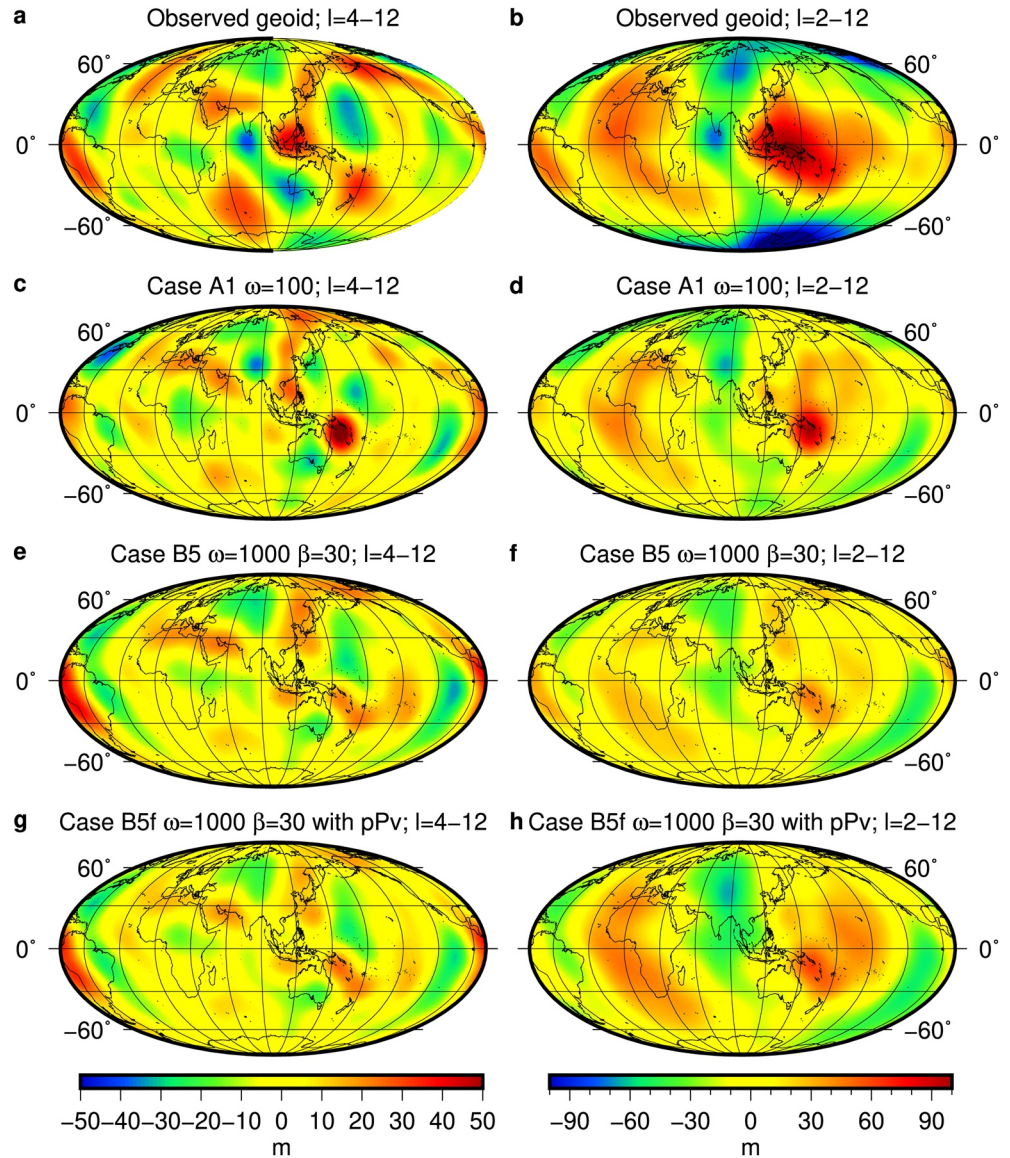
Figure 3. Geoid maps at degrees 4–12 (left figures) and 2–12 (right figures). Panels a–b, c-d, e-f and g-h are the observed geoid, the modeled geoid of Cases A1 ($\omega = \eta_{LM} / \eta_{UM} = 100$), B5 ($\omega = \eta_{LM} / \eta_{Asth} = 1000$, $\beta = \eta_{LM} / \eta_{TZ} = 30$), and B5 with viscosity reduction due to Pv-pPv phase transition, respectively.

reductions between Cases A2–A6 and the observed are all worse than those of Case A1 (Figure 4, black circles). To evaluate the effect of viscosity and buoyancy structure separately, we also calculate the geoid by using the present-day buoyancy structure in Case A1 but with ω as those in Cases A2–A6 (Figure 4, black squares). On the one hand, for a given viscosity ratio ω, the geoid correlations at degrees 4–12 are higher for models using the buoyancy structure from Case A1 than those from Cases A2–A6, suggesting that Case A1 with $\omega = 100$ generates buoyancy structure that could fit the geoid better than that from Cases A2–A6. On the other hand, when fixing the buoyancy structure from Case A1 with varying viscosity ratio ω, the best-fit geoid still occurs at $\omega = 100$ for Case A1, suggesting that $\omega = 100$ is the optimal viscosity ratio that dynamically produces thermal and buoyancy structures that fit the geoid for the three layer models.

Case A7 is identical to Case A1 except the weak layer beneath the spinel-to-post-spinel phase transition is a global weak layer as in MZ18 and MZ19 (Figure S1) instead of a regional weak layer as in Case A1. Case A7 shows nearly identical slab structures as in Case A1, indicating that only the weak layer below subduction zones affects slab structures (e.g., leading to stagnant slabs). However, the geoid correlations and
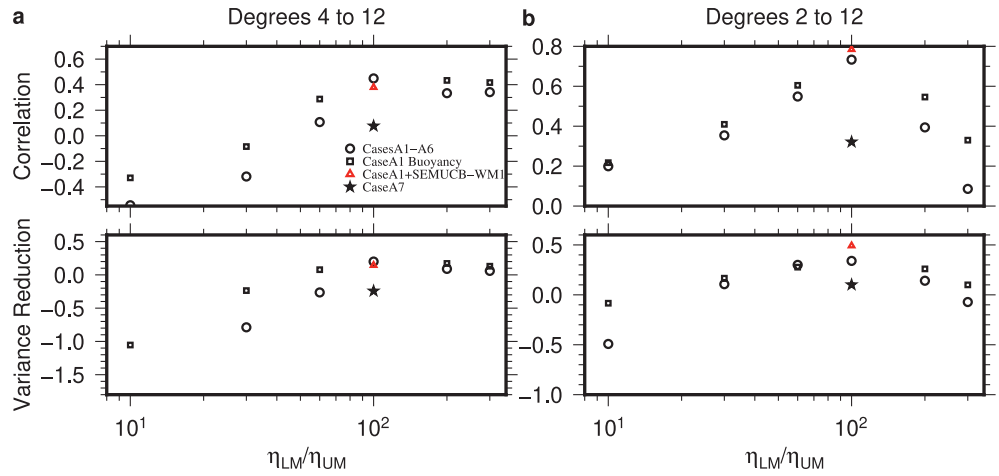
Figure 4. Correlations (top figures) and variance reductions (bottom figures) between the modeled and observed geoid at degrees 4–12 (left) and 2–12 (right) for three-layer models with different η_{LM} / η_{UM} (Cases 1–7). For the modeled geoid, the buoyancy structures used in the black circles, black squares, red triangles, and black stars are from Cases A1–A6, Case A1, combination of buoyancy from Case A1 above 1,500 km depth and that converted from SEMUCB-WM1 below 1,500 km, and Case A7, respectively.
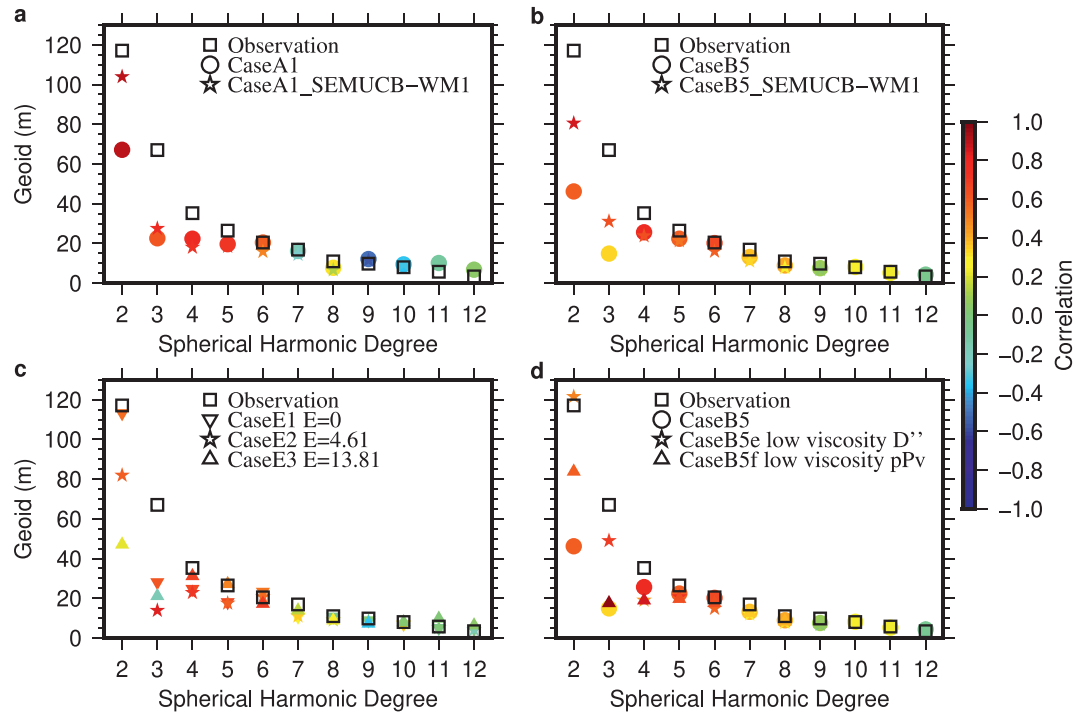
Figure 5. The square root degree-power of geoid. (a) The squares, circles, and stars are for the observed geoid, the modeled geoid of Case A1, and combination of buoyancy from Case A1 above 1,500 km depth and that converted from SEMUCB-WM1 below 1,500 km, respectively. (b) The squares, circles, and stars are for the observed geoid, the modeled geoid of Case B5, and combination of buoyancy from Case B5 above 1,500 km depth and that converted from SEMUCB-WM1 below 1,500 km, respectively. (c) The squares, inverted triangles, stars and triangles are for the observed geoid, and the modeled geoid of Cases E1, E2, and E3, respectively. (d) The squares, circles, stars, and triangles are for the observed geoid, the modeled geoid of Case B5, Case B5 with a low viscosity D″ layer and Case B5 with reduced viscosity due to Pv-to-pPv phase transition, respectively.

variance reductions of Case A7 are all significantly reduced (Figure 4, black stars) compared with those for Case A1 (Figure 4, black circles). Note that such a global weak layer below the 670 km phase change has been used in the geoid modeling (e.g., Mitrovica & Forte, 2004). Comparison of the geoid modeling for Cases A7 and A1 here suggests that the regional weak layer below subducted slabs may lead to a better geoid fit.

3.2. Four Layer Models

3.2.1. Weak Asthenosphere

The weak asthenosphere underneath the lithosphere has ubiquitous effects on dynamic process of the mantle (e.g., Becker, 2017; Richards & Lenardic, 2018; Semple & Lenardic, 2020). To investigate its effects on the geoid, we formulate Cases B1–B7 with four viscosity layers by including an additional layer of asthenosphere that extends from the base of lithosphere to 300 km depth (Table 2). In Cases B1–B7, $\beta = \eta_{LM} / \eta_{TZ}$ is fixed at 30, while $\omega = \eta_{LM} / \eta_{Asth}$ are 100, 200, 300, 600, 1,000, 2,000, and 3,000, respectively (Figure 1b). For Cases B6 and B7 with ω of 2,000 and 3,000, to maintain coherent slab structures in the asthenosphere, we increase the viscosity of cold slabs in the asthenosphere by 10 times in addition to the temperature-dependent viscosity. Figure 6a shows the geoid correlations and variance reductions to the observed geoid for these seven models. The correlations for degrees 4–12 of Cases B4–B5 are the highest with both at 0.61, and the corresponding variance reductions are both 0.37, representing significant improvement over Case A1 (Figures 4a and 6a). Both Cases B4 and B5 produce slab structures (Figure 7 for Case B5) that are similar to the seismic slabs and also those in Case A1 (Figure 2) except that the slabs in Case B5 are thinner in the asthenosphere due to the small viscosity. The overall geoid pattern of Case B5 (Figures 3e and 5b) is also similar to that of Case A1 (Figures 3c and 5a), and the main difference appears to be that the geoid highs in the western Pacific subduction zones are closer to the trenches in Case B5 than in Case A1.

Cases B8–B10 are identical to Case B5 (i.e., $\omega = \eta_{LM} / \eta_{Asth} = 1000$) except that the mantle transition zone viscosity is different with $\beta = \eta_{LM} / \eta_{TZ}$ that changes from 30 in Case B5 to 10, 60, and 100, respectively (Table 2). These cases show smaller correlations and variance reductions to the observed geoid than Case B5, especially at degrees 2–12 (Figure 6b).

The dynamic geoid is always associated with dynamic topography (e.g., Hager & Richards, 1989). The topography for both Cases A1 and B5 display clear signals associated with mid-ocean ridges and trenches (Figures 8a and 8c), and this is expected because our model with realistic plate motions produces realistic age-dependent lithospheric thermal structure and subducted slabs. Another clear pattern is the negative (positive) topography in continental (oceanic) regions. This is due to our model setup in that our model non-subducting continental lithosphere is generally older hence colder than oceanic lithosphere and also model lithosphere excludes the crust. This result is similar to that in Zhang et al., (2012) who performed similar calculations of topography from convection models with longer duration plate motions. However, Zhang et al. (2012) did not compute the geoid and their model resolution was significantly less than in the current study.

Following Zhang et al. (2012), we did another calculation of the geoid and topography for Cases A1 and B5 in which the same present-day viscosity and buoyancy structures are used, except that the top 200 km of the mantle buoyancy (i.e., the lithosphere buoyancy) is removed. The resulting topography would not include lithospheric contribution and can be considered as true dynamic topography (e.g., Hager & Richards, 1989; Molnar et al., 2015; Zhang et al., 2012). Both Cases A1 and B5 show relatively small amplitude (0.5–0.8 km) of surface dynamic topography above the Pacific and African LLSVPs (i.e., mostly degree-2) that is only about half to two thirds of that in previous models that considered the upwelling buoyancy structures (e.g., Flament et al., 2013; Hager & Richards, 1989; Liu & Zhong, 2016; Yang & Gurnis, 2016). The relatively small amplitude of dynamic topography in the Pacific and African regions in Cases A1 and B5 may be related to relatively small amplitude of long-wavelengths (degrees 2 and 3) geoid (Figure 5), compared with the observed.

The surface topography for Case B5 with a weak asthenosphere is uniformly smaller than that of Case A1 at degrees 1–12 (Figure 8e), but how the dynamic topography is related between Cases B5 and A1 is more
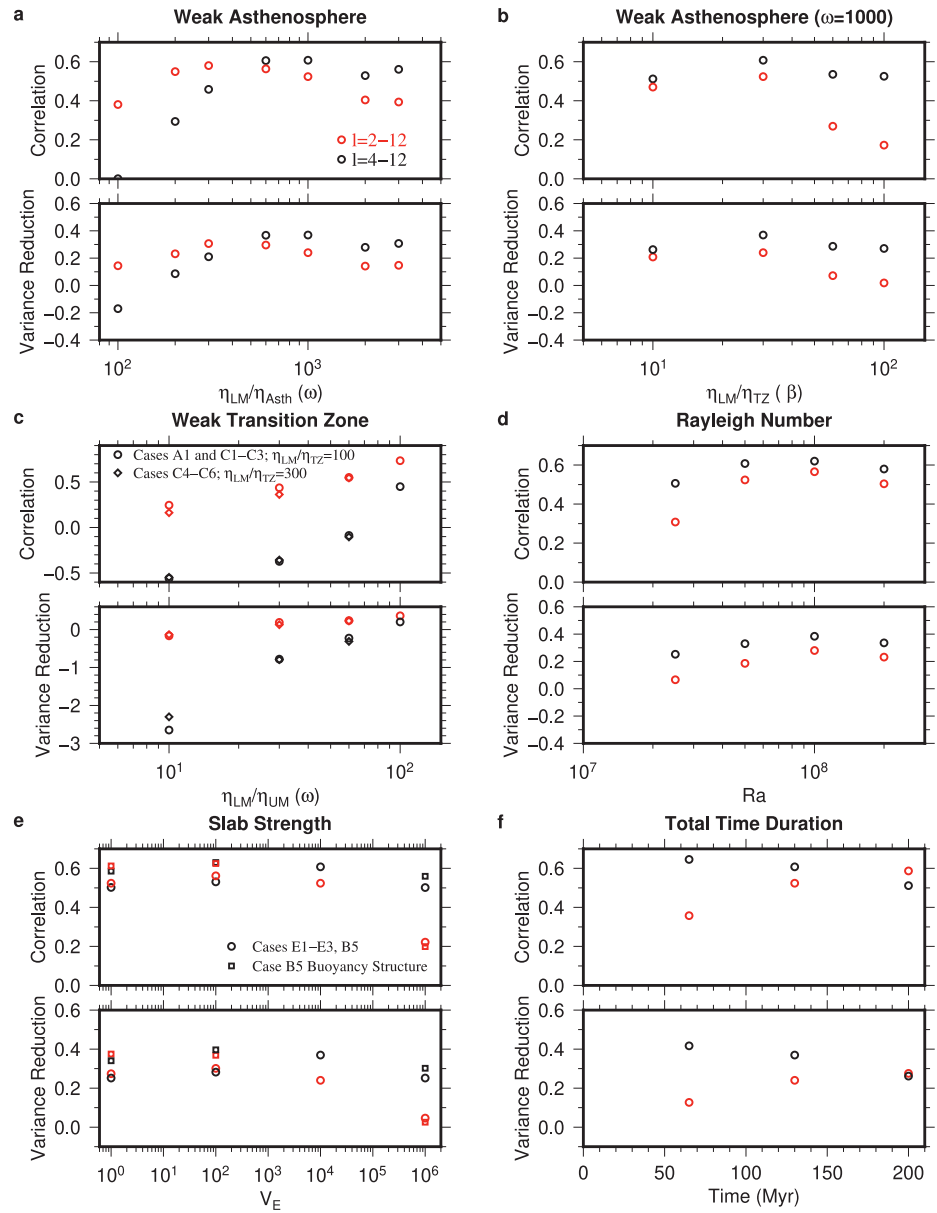
Figure 6. Correlations (top figures) and variance reductions (bottom figures) between different series of the modeled and observed geoid at degrees 2–12 (red) and 4–12 (black). (a) The modeled geoid are from Cases B1–B7 with different $\omega = \eta_{LM} / \eta_{Asth}$. This set of models are used to test the effects of the weak asthenosphere. (b) The modeled geoid are for Cases B5 and B8–B10 with different $\beta = \eta_{LM} / \eta_{TZ}$ while $\omega = \eta_{LM} / \eta_{Asth}$ is fixed at 1,000. (c) The modeled geoid are for Cases A1, C1–C3 (circles) with $\beta = 100$ and different ω, and C4–C6 (diamonds) with $\beta = 300$ and different ω. This set of models are used to test the effects of the weak transition zone. (d) The modeled geoid are for Cases B5 and D1–D3 with different Ra. (e) The modeled geoid are for Cases B5 and E1–E3 with different activation energy E (circles). The squares are for cases with the same buoyancy structure of Case B5 while varying E. (f) The modeled geoid are for Cases B5, F1, and F2 with different total time duration.

complicated. Compared with Case A1, the dynamic topography for Case B5 is larger at degrees 1, 3, and 4, similar at degrees 2, 5, and 6, but considerably smaller at degrees 7–12 (Figure 8f). Although a weak asthenosphere may cause dynamic topography to decrease (e.g., Molnar et al., 2015; Morgan, 1965), our calculations here show that such an effect is only pronounced at intermediate wavelengths. This may result from different convective thermal buoyancy structures in models with different asthenospheric viscosity.
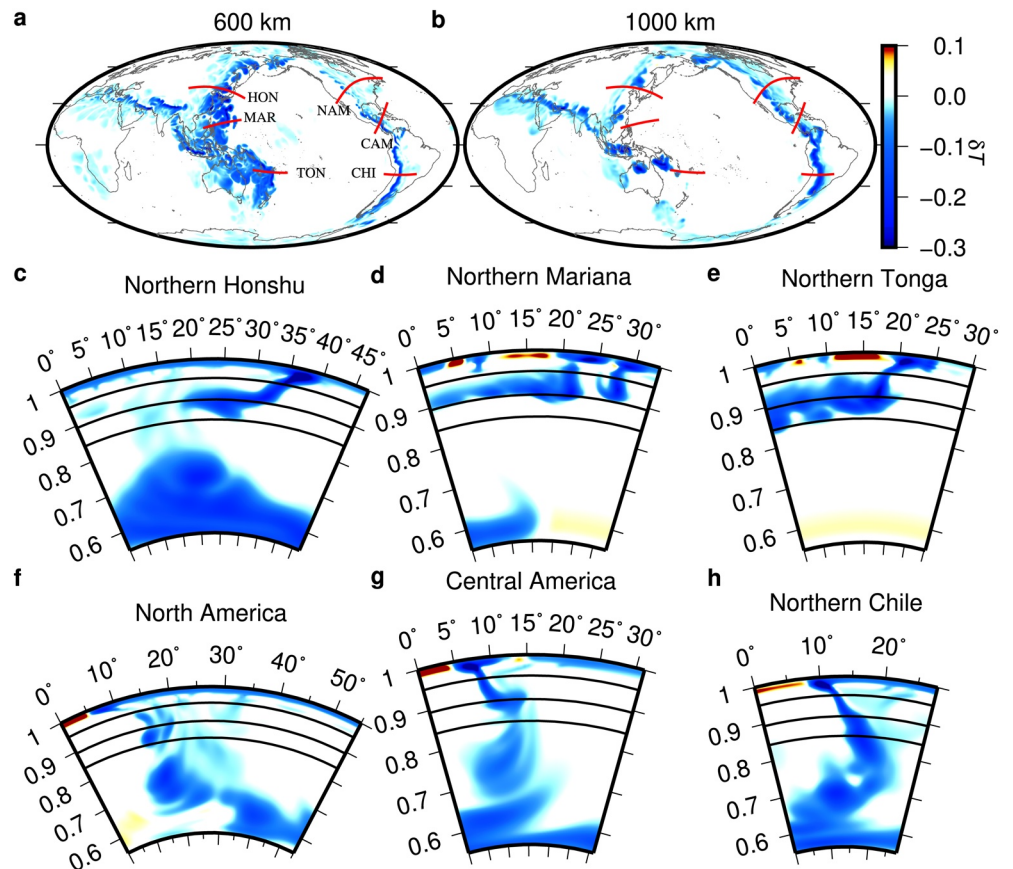
Figure 7. Present-day dimensionless temperature anomalies (δT) of Case B5.

3.2.2. Weak Transition Zone

The mantle transition zone is also suggested to be weak (e.g., Bercovici & Karato, 2003; Nestola & Smyth, 2015; Williams & Hemley, 2001) due to potentially high water content. Previous geoid studies (Liu & Zhong, 2016; Steinberger & Calderwood, 2006) showed that with mantle buoyancy derived from seismic tomography models a weak mantle transition zone would even lead to a marginally better fit to the geoid, while the existence of a weak transition zone is still debatable (Lee et al., 2011; Wang et al., 2019). It is therefore interesting to examine whether a weak mantle transition zone would result in dynamically generated thermal (buoyancy) structure for the present-day mantle that improves the geoid fit. Additionally, it is also interesting to examine whether a weak transition zone could help channel slabs to form stagnant slabs there.

We formulate Cases C1–C6 with a weak transition zone (Table 2). Cases C1–C3 have the same transition zone viscosity as Case A1 with $\beta = \eta_{LM} / \eta_{TZ} = 100$ but the upper mantle has a larger viscosity with ω that are 10, 30 and 60, respectively; while Cases C4–C6 have weaker transition zone with β of 300 and $\omega = \eta_{LM} / \eta_{Asth}$ that are 10, 30, and 60, respectively. That is, Cases C1–C3 have the same transition zone viscosity but larger upper mantle viscosity, compared with Case A1, while Cases C4–C6 have an even weaker transition zone. Also note that no asthenosphere is included in Cases C1–C6. Cases C4–C6 show that the weak transition zone does not appear to promote additional slab stagnation in the transition zone strongly (Figure S4). In addition, the geoid fit at degrees 4–12 for Cases C1–C6 are significantly worse than that for Case A1 or Case B5 (Figure 6c, circles for Cases C1–C3 and diamonds for Cases C4–C6).
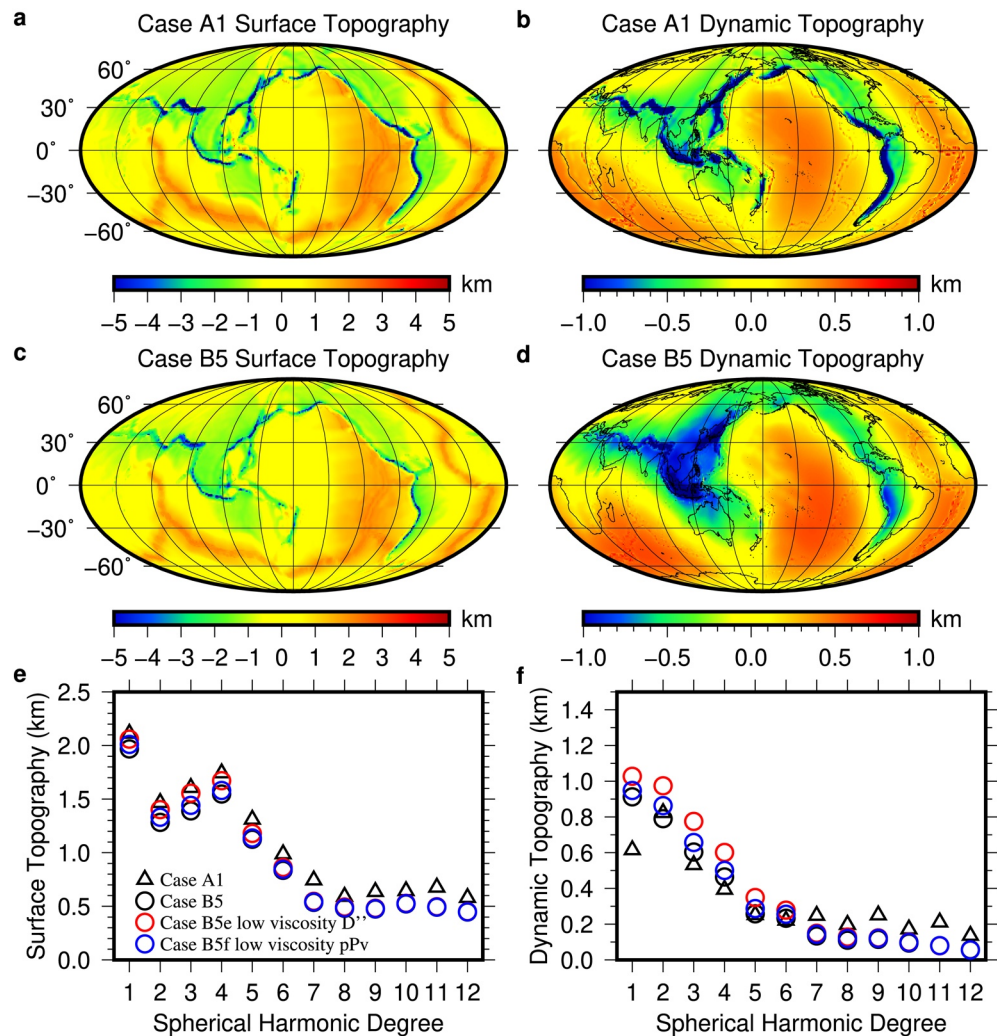
Figure 8. Surface topography, dynamic topography (i.e., excluding the contribution from the buoyancy of the top 200 km), and the corresponding power spectra for Cases A1 and B5. The black triangles, black circles, red circles, and blue circles in panels (e)–(f) are for Cases A1, B5, B5 with a low viscosity D″ layer, and B5 with viscosity reduction due to Pv-pPv phase transition.

3.3. Rayleigh Number

For a given buoyancy structure (e.g., that derived from seismic models), the geoid is only sensitive to the relative viscosity distribution but not the absolute viscosity (e.g., Hager & Richards, 1989). However, the absolute value of viscosity determines the effective Rayleigh number that controls the mantle flow velocity and buoyancy structure. Therefore, the geoid could be strongly affected by the Rayleigh number due to its influence on buoyancy structure. We compute Cases D1–D3 that are identical to Case B5 ($Ra = 5 \times 10^7$, a four layer viscosity model with a weak asthenosphere) except that Ra are 2.5×10^7, 10^8, and 2×10^8, respectively (Table 2). The corresponding reference lower mantle viscosity η_{LM} of Cases B5, D1–D3 are 2.5×10^{22}, 5.0×10^{22}, 1.3×10^{22}, and 6.3×10^{21} Pa·s, respectively. Case D1 with the smallest Ra leads to the thickest slabs and also unrealistic slab distribution in the mantle transition zone near Antarctica (Figures S5a–S5c), which is due to subduction between 120-100 Ma near Antarctica, whereas slabs subducted in this time interval have sunk to the lowermost mantle for other cases (Figures S5h and S5l; also see Figure S7 of MZ18). While Cases D2 and D3 with larger Ra than Case B5 result in thinner slabs (Figures S5e–S5l). Compared with Case B5, while Cases D1 and D3 show significantly worse geoid results at degrees 4–12, Case D2 shows comparable geoid correlations and variance reductions (Figure 6d). Note that our previous studies in MZ18

and MZ19 show that convection models with $Ra = 5 \times 10^7$ (i.e., the same as for Case B5) also show better correlations with seismic tomographic models.

3.4. Slab Strength

Slab strength could strongly affect the couplings among the slabs, the lithosphere and CMB and also slab structure evolution, thus affecting the surface and CMB topographies and the geoid (Billen et al., 2003; Billen & Gurnis, 2001; Moresi & Gurnis, 1996; Tosi, Čadek, & Martinec, 2009; Yang & Gurnis, 2016; Zhong & Davies, 1999; Čadek & Fleitout, 2003). We compute Cases E1–E3 that are identical to Case B5 ($E = 9.21$), except that Cases E1–E3 have activation energy E below the lithosphere of 0, 4.61, and 13.82, respectively (Table 2), while E is kept the same for the lithosphere for all these cases. The corresponding total viscosity contrast V_E for Cases E1, E2, B5, and E3 would be 1, 10^2, 10^4, and 10^6, respectively. Slabs in Cases E1 and E2 are ~100 and ~10 times weaker than those in Case B5 and they appear to be less coherent and more dispersed than in Case B5 (Figures S6a–S6h, 7c–7d and 7f–7g). These weaker slabs appear to be less affected by and easier to penetrate through the 670 km phase transition, especially in the northern Honshu subduction zone (Figures S6a and S6e). The more dispersed (i.e., thicker) and weaker slabs result in larger amplitudes of geoid at degree 2 (Figure 5c, inverted triangles and stars for Cases E1 and E2, respectively). Case E1′s degree 2 amplitude is nearly the same as the observed, compared with Case B5. However, the geoid correlations and variance reductions of Cases E1 and E2 to the observed geoid at $l = 4$–12 are worse than those of Case B5 (Figure 6e, circles). Case E3 with slabs which are ~10 times stronger than those in Case B5 shows similar slab structures as in Case B5 (Figures S6i–S6l), but both the correlations and variance reductions to the observed geoid at $l = 4$–12 are significantly lower than those of Case B5 (Figure 6e, circles). Using the present-day buoyancy structure in Case B5 while varying E as in Cases E1–E3 results in improved fit of geoid and the best fit is achieved at $E = 4.61$ and 9.21 (Figure 6e, circles for $V_E = 10^4$ and squares for other cases).

3.5. Total Time Duration

We also formulate models with different time durations of plate motion history. Cases F1 and F2 have the model time durations of 65 and 200 Myr, respectively, but they are otherwise identical to Case B5 that is computed for 130 Myr (Table 2). Compared with Case B5, Case F1 with 65 Myr model time duration shows slightly higher correlations and variance reductions with the observed geoid at $l = 4$–12, while Case F2 with 200 Myr time durations results in reduced correlation and variance reduction (Figure 6f). The geoid anomalies at intermediate wavelengths are mostly sensitive to structures in the upper mantle and the uppermost lower mantle (e.g., Hager, 1984). Our previous studies in MZ19 demonstrated that with 65 Myr plate motion history, the convection models could reproduce well seismically fast anomalies (i.e., slabs) above ~1,500 km depth, although the models fail in explaining mantle structures at larger depths. Therefore, the slab structures from all these three cases are similar to each other at depths less than 1,500 km, leading to similar geoid anomalies and reasonably good geoid fit at degrees 4–12. However, with longer model time durations as in Case F2, the uncertainties in plate motion and also other processes like sub-lithospheric small-scale convection and lower mantle flows may lead to the mantle structure and geoid signals that are inconsistent with the observed.

3.6. Plate Margin Viscosity, Plate Motions and Geoid

In modeling the present-day geoid, we replace the velocity boundary conditions at the surface (i.e., plate motions) with a free-slip boundary condition, together with reduced viscosity for plate margins for the final step of each time-dependent model, as discussed in Section 2.4. Specifically, the width of plate margins is taken to be 200 km, and the viscosity of plate margins is either reduced to uniformly low values (e.g., 1/15 or 1/60, regardless of temperature) or further finetuned based on plate motion speed, while the viscosity outside plate margins is kept unchanged (Figures 9e–9h). The plate margin viscosity is chosen such that the resulting flow velocities at the surface are consistent with observed plate motions.

For the four-layer model Case B5 with a weak asthenosphere, surface motion increases with decreasing plate margin viscosity, as expected (Figures 9a and 9b for surface motions and observed plate motions for
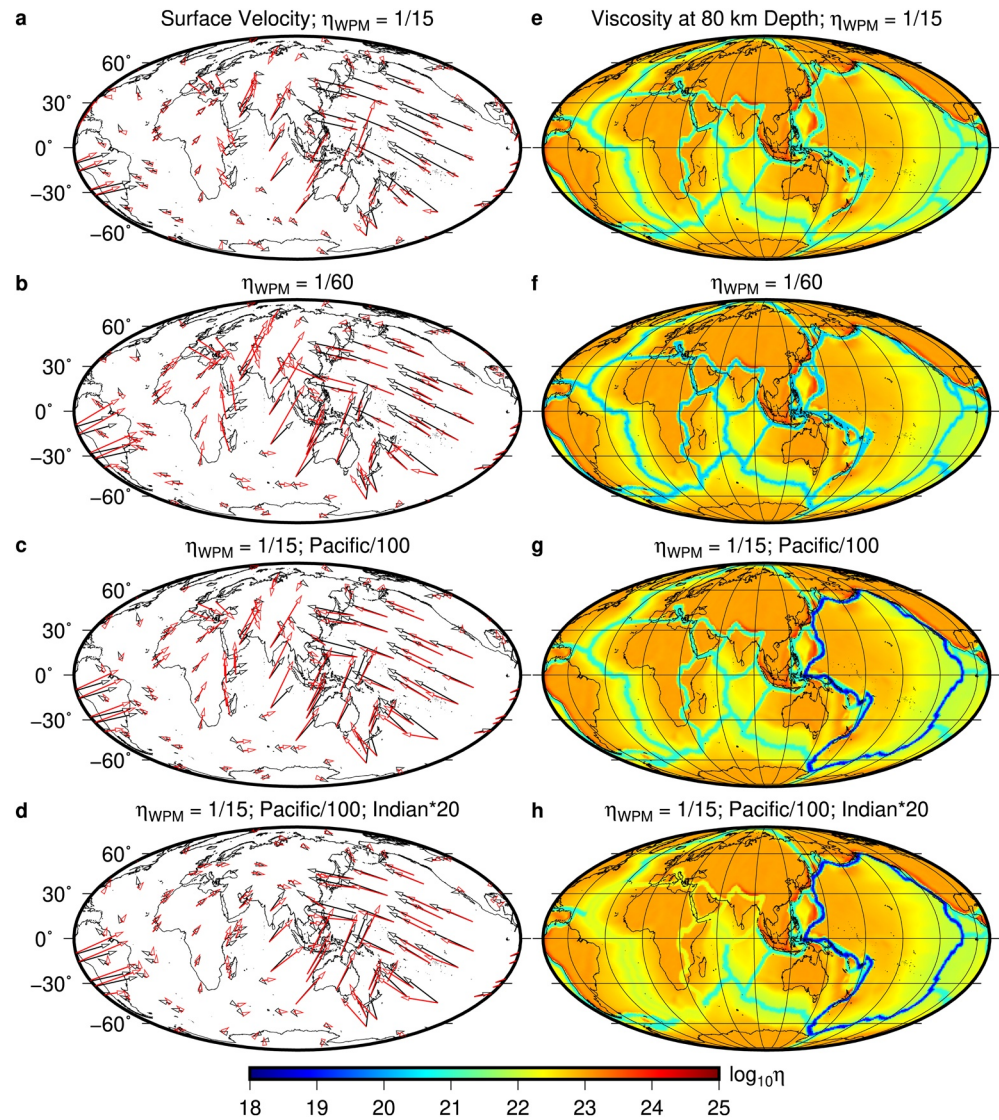
Figure 9. The observed (black arrows) and modeled (red arrows) surface velocity field, and the corresponding viscosity at 80 km depth. The observed surface velocity field is in a hotspot reference frame (O'Neill et al., 2005; Seton et al., 2012). Panels (a) and (e) are for Case B5a with dimensionless viscosity of 1/15 at plate margins. Panels (b) and (f) are for Case B5b with dimensionless viscosity of 1/60 at plate margins. Panels (c) and (g) are for Case B5c which is identical to Case B5a except the viscosity at the plate margin of the Pacific Plate is 1/1,500. Panels (d) and (h) are for Case B5d which is identical to Case B5c except the viscosity at the plate margins of the African, Indian, and Arabian Plates is 4/3 (marked as Indian*20 in the figure). Note that in Figure 9h the viscosity of the mid-Atlantic ridge is slightly higher than its ambient mantle, because the viscosity is plotted for 80 km depth and below the lithosphere. At shallow depths in the lithosphere, the mid-ocean ridge viscosity remains much smaller than that of the lithosphere.

two calculations Cases B5a and B5b in which plate margin viscosity is set at a dimensionless constant value of 1/15 and 1/60, respectively). While the correlation between the modeled and observed poloidal motion is remarkably high (>0.9) regardless of plate margin viscosity (Figure 10a), the large variance reduction (~0.8) only occurs when the plate margin viscosity is smaller than 1/60 (e.g., Case B5b) (Figure 10d). However, the correlation and variance reduction for toroidal motion are significantly worse than those for poloidal motion (Figures 10b and 10e). Examining the modeled and observed spectra of the poloidal and toroidal motions (Figure 11) reveals the causes of the discrepancy. While the spectra of model poloidal motion generally follow that of the observed (Figures 11a), the spectra of model toroidal motion for Cases B5a and B5b show much smaller amplitude at degrees 1 and 2 than those of the observed (Figures 11b). Other calculations with larger plate margin viscosity than Cases B5a and B5b show even smaller toroidal motions and worse
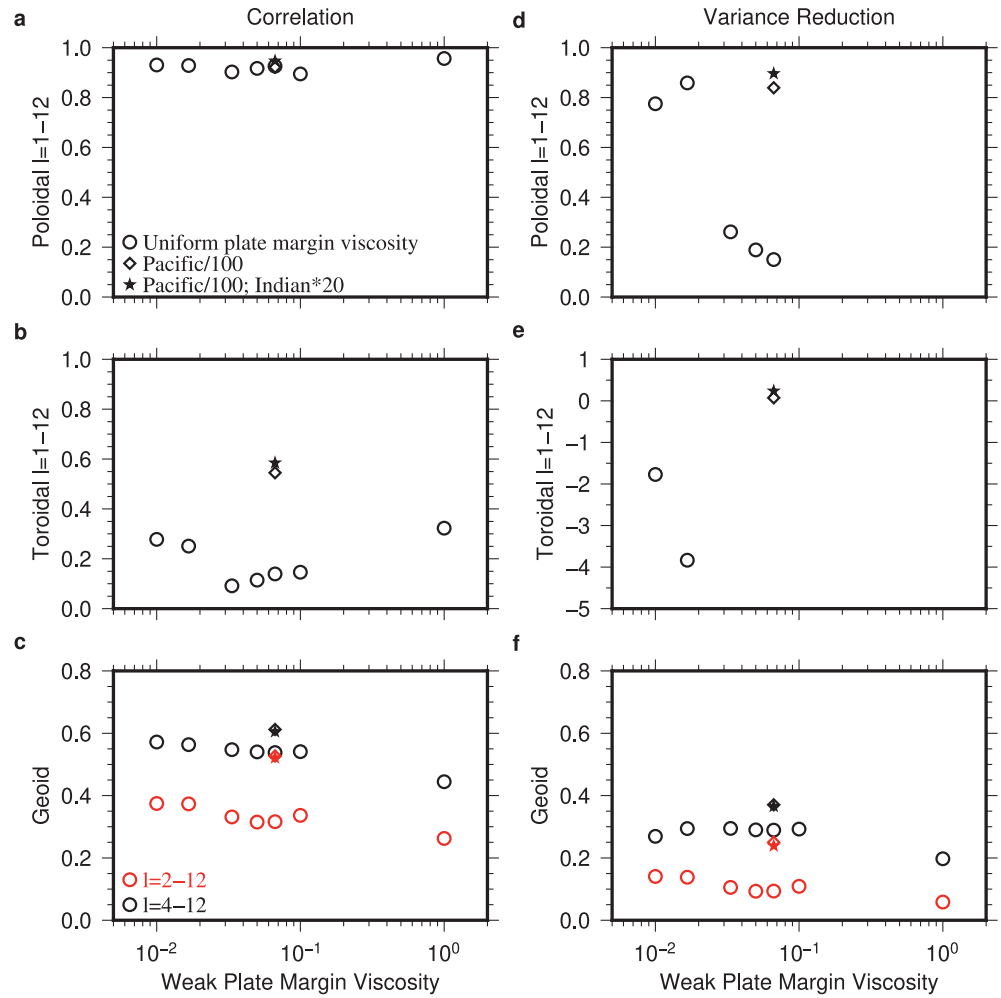
Figure 10. The correlations and variance reductions between the observed and modeled poloidal and toroidal plate motions, and geoid (red for $l = 2$–12 and black for $l = 4$–12) for models with different plate margin viscosity structures. The circles are for Case B5 with different plate margin viscosities. The diamonds and stars are for Cases B5c and B5d, respectively. Note in panels (d) and (e), the variance reductions for models with moderately weak plate margins are too strongly negative to show here.
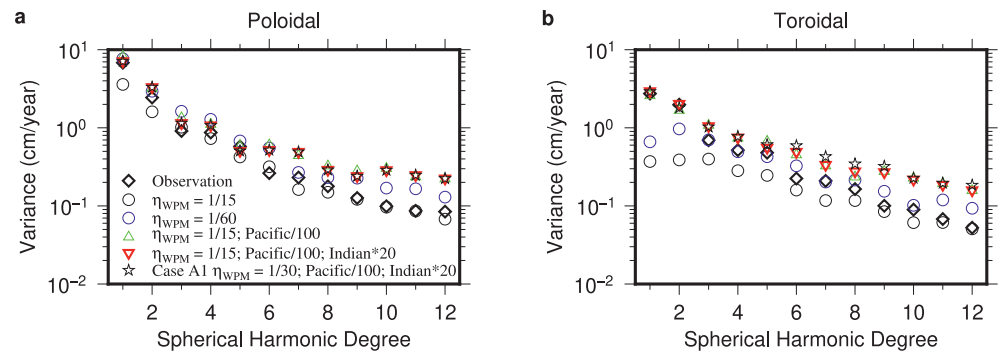

Figure 11. Degree variances for (a) poloidal and (b) toroidal plate motions. The black diamonds, black circles, blue circles, green triangles, red inverted triangles, and black stars are for the observed, Cases B5a, B5b, B5c, B5d, and best fit model of Case A1.

variance reductions (Figure 10e), even though some may display reasonable correlations (Figure 10b). The lack of degree-1 toroidal motion (i.e., no net rotation of lithosphere) with uniformly weak plate margins is the same as reported in Zhong (2001).

We now consider model calculations with non-uniform plate margin viscosity (Figures 9g and 9h). Notice that for Case B5b with the plate margin viscosity of 1/60, although the poloidal motion is larger than the observed (Figure 11a), the Pacific Plate moves significantly slower, while the Indian and African Plates move much faster, than the observed (Figure 9b). This motivates us to consider two additional calculations Cases B5c and B5d in which the viscosity is different for the plate margins surrounding the Pacific, African and Indian Plates, while the viscosity for other plate margins is fixed at 1/15 (Figures 9g and 9h). In Case B5c, the plate margin viscosity for the Pacific Plate is reduced by an additional factor of 100 to 1/1,500, and the resulting plate motion is in a much better agreement with the observed, particularly for the Pacific Plate and its surrounding plates (Figure 9c). Importantly, this leads to significant improvement in toroidal motions, particularly its degree-1 component or the net rotation of lithosphere (Figures 10b, 10e, and 11b). In Case B5d, the viscosity at the plate margins of the African, Indian and Arabian Plates is increased by 20 times to 4/3, in addition to the reduced viscosity for the Pacific Plate margins (Figure 9h, and note that the mid-Atlantic ridge shows slightly higher viscosity than its ambient mantle, because the viscosity is plotted for 80 km depth beneath the ridge). For this case, African and Indian plate motions are further improved, so are the toroidal motions (Figures 9d, 10a, 10b, 10d, 10e, and 11b). We also compute a case that is identical to Case B5d except that the viscosity is increased only at the subduction zones of the African, Indian and Arabian Plates. The model African and Indian plate motions do not match the observed as well as in Case B5d, but the global properties of plate motions as in Figures 9d, 10, and 11 only have negligibly small changes.

Reducing plate margin viscosity leads to slightly improved fit to the geoid (i.e., increased correlation and variance reduction; Figures 10c and 10f). Importantly, plate margins with variable viscosities in Cases B5c and B5d tend to produce the best geoid correlation and variance reduction to the observed, in addition to reproducing the observed plate motions. Therefore, all the geoid models with a weak asthenosphere with $\omega = \eta_{LM} / \eta_{Asth} \geq 600$ (Table 2) use the plate margin viscosity in Case B5d (i.e., Figure 9h). For Case A1 with $\omega = 100$ (Table 2), by doing similar tests as those for Case B5, we found that reducing plate margin viscosities by a factor of 2 relative to those for Case B5d provides optimal fits to the observed plate motions (Figure 11) and the geoid. This plate margin viscosity model is used for all the geoid models with $\omega \leq 300$ (Table 2).

4. Discussions

4.1. Mantle Buoyancy Structure, Geoid, and Mantle Viscosity

The geoid highs over subduction zones (i.e., for $l \geq 4$) have been proposed to be mostly related to subducted slabs in the top half of the mantle, and to require a viscosity increase from the upper mantle to lower mantle (e.g., Hager, 1984; Hager & Richards, 1989). Previous studies on the geoid have used mantle buoyancy derived from either slab density models (e.g., Lithgow-Bertelloni & Richards, 1998; Ricard et al., 1993), or seismic models (e.g., Ghosh et al., 2017, 2010; Hager & Richards, 1989; Liu & Zhong, 2016; Rudolph et al., 2015; Spasojevic et al., 2010; Yang & Gurnis, 2016), or a combination of slab and seismic models (e.g., Hager, 1984; Hager & Richards, 1989). While these models successfully reproduce long-to intermediate-wavelength (degrees 2–12) geoid anomalies, it remains unclear whether the inverted viscosity structures are dynamically consistent with the buoyancy structures that are used in these instantaneous flow models. The question on dynamical consistency is important, as demonstrated by our model calculations of Cases A1–A6 with different η_{LM} / η_{UM} in that while these cases produce significantly different thermal/buoyancy structures (Figures 2 and S3, also see MZ18 and MZ19) and fits to the observed geoid (circles in Figure 4), for a fixed buoyancy structure a similar geoid can be obtained for quite different viscosity structures for degrees 4–12 (squares with $\eta_{LM} / \eta_{UM} = 200$ and 300, and circles with $\eta_{LM} / \eta_{UM} = 100$ in Figure 4).

In this study, we present the first time-dependent mantle convection models with surface plate motion history and realistic lithospheric viscosity that produce present-day mantle thermal and buoyancy structures with mantle viscosity structures that dynamically consistently reproduce both seismic slab structures and intermediate-wavelengths geoid anomalies ($l = 4$–12). As demonstrated in MZ19, the convection models show relatively good correlations with seismic tomographic models to spherical harmonic degrees 20, espe-

cially above ∼800 km depth. Considering three-layer models, the best fit model is Case A1 in which the lower mantle viscosity is 100 times larger than that in the upper mantle, which is within the range of previous geoid and glacial isostatic adjustment studies (e.g., Hager, 1984; Mitrovica & Forte, 2004). When applying four-layer models with an additional layer of asthenosphere (from 130 to 300 km depths), the best fit models are Cases B4 and B5 where the lower mantle viscosity is ∼30 and 600–1,000 times higher than that in the transition zone and asthenosphere, respectively. The geoid correlations and variance reductions for degrees 4–12 of Cases B4–B5 are both at 0.61 and 0.37, respectively (Figure 6a), which are significantly better than those for Case A1 with no asthenosphere (Table 2). Therefore, the geoid anomalies over subduction zones for degrees 4–12 strongly suggest the existence of a weak asthenosphere between 130 and 300 km depths.

Based on both slab structures and the subduction zone geoid of degrees 4–12, our preferred lower mantle viscosity is ∼1.3–2.5 × 10²² Pa·s (i.e., Figure 1b, using Ra for our best fit models Cases B4–B5, and D2 and model parameters in Table 1), which is consistent with glacial isostatic adjustment studies (e.g., Mitrovica, 2004). This suggests that the asthenospheric viscosity is in the range of ∼1.3–4.2 × 10¹⁹ Pa·s, which is similar to that inferred in Becker (2017) and Wang et al. (2019). Such a weak asthenosphere may have important implications for sub-lithospheric small-scale convection in mantle dynamics (e.g., Huang & Zhong, 2005) and glacial isostatic adjustment process. Compared with previous geoid studies that used buoyancy structures from either a slab density model (Lithgow-Bertelloni & Richards, 1998) or seismic models (Liu & Zhong, 2016 for S40RTS [Ritsema et al., 2011] and SEMUCB-WM1 [French & Romanowicz, 2014, 2015]; Figure S7), our best fit model Case B5 shows similarly good geoid correlation (Figure S7a) and comparable geoid amplitude (Figure S7b) at intermediate wavelengths of degrees 4–12.

The endothermic spinel-to-post-spinel phase transition at ∼670 km depth in our models provides positive buoyancy that promotes slab stagnation in the mantle transition zone above the lower mantle, as observed in the western Pacific and other subduction zones in seismic tomographic models (e.g., Fukao & Obayashi, 2013), and also affects the subduction zone geoid. Although the inclusion of the phase transition buoyancy, together with trench migration, is crucial in reproducing stagnant slab structures (e.g., Christensen, 1996; Zhong & Gurnis, 1995), it does not eliminate the need for viscosity increase from the transition zone to the lower mantle to reproduce positive geoid at subduction zones as indicated by King (2002). We also formulate a test calculation that uses the present-day thermal structure and viscosity from Case B5, but removes the phase change buoyancy. The correlation of the test calculation at degrees 4–12 slightly increases from 0.61 to 0.64, and the variance reduction increases from 0.37 to 0.41, compared with Case B5. While this test calculation excluding the phase change buoyancy improves the geoid fit, MZ18 and MZ19 demonstrated that models without the phase change fail to reproduce the stagnant slab structures. Considering the large uncertainties in conversion of seismic velocity anomalies to mantle buoyancy, it remains a significant challenge to implement phase change buoyancy from seismic tomographic models.

4.2. Weak Plate Margins, Surface Plate Motion, and the Geoid

An important characteristic of plate tectonics is that the plate interiors are strong while plate margins are weak due to faulting, partial melting, and possibly grain-size dependent and non-linear viscosity (e.g., Bercovici, 2003). Previous studies indicate that this characteristic of strong plate interiors and weak plate margins is crucial in reproducing the geoid and plate motion simultaneously (Ghosh et al., 2010; Tosi, Čadek, & Martinec, 2009; Zhong, 2001; Zhong & Davies, 1999), specifically the "plate-like" motion (i.e., nearly rigid plate motion with deformation only occurring at plate margins; e.g., King et al., 1992; Zhong & Gurnis, 1996) and long-wavelength geoid (Zhong & Davies, 1999). Our current study with weak plate margins and time-dependent convection models largely confirms these previous studies. However, our study sheds some new insight into weak plate margins' roles in influencing the geoid and plate motion.

The new results are related to the effects of non-uniform viscosity of plate margins (i.e., the non-uniform coupling at plate margins) on the geoid and plate motions. Although previous studies demonstrated the important effects of weak plate margins on improving the geoid fit at long-wavelengths including degree-2 (e.g., Zhong & Davies, 1999), these models with uniformly reduced viscosity at plate margins fail to produce any significant net rotation of lithosphere (i.e., degree-1 toroidal motion) (Zhong, 2001; Becker, 2006), which is an important feature of the present-day plate motion in a hot-spot reference frame (e.g., Gripp & Gordon, 2002). Previous studies have suggested that continental keels (Zhong, 2001; Becker, 2006; Ru-

dolph & Zhong, 2014), effective coupling of oceanic plates (e.g., the Pacific Plate) to the mantle via the slabs (Conrad & Lithgow-Bertelloni, 2002), and the geometry and viscosity of the slabs and weak zones (Gérault et al., 2012) may cause net rotation of lithosphere. Our current study shows that non-uniform plate margin viscosity (e.g., much weaker plate margins surrounding the Pacific Plate but relatively strong plate margins for the Africa, India and Arabia Plates) is effective in generating net rotation of lithosphere (Figures 9d, 9h, 10b, 10e, and 11b). Additionally, this non-uniform plate margin viscosity also leads to much better geoid fit to the observed, especially for degrees 2–3, compared with uniform plate margin viscosity (Figures 10c and 10f). Importantly, plate margin effective viscosity inferred from observed strain-rate (e.g., Ghosh et al., 2013; Ghosh & Holt, 2012; Kreemer et al., 2003) is consistent with our non-uniform plate margin viscosity. This result has important implications for understanding lithospheric net rotation for not only the present-day but also for the past plate motions (e.g., Rudolph & Zhong, 2014).

4.3. The Effects of Lateral Variation in Viscosity on the Geoid

The lateral variations in viscosity (LVV) in the mantle, especially the viscosity contrast between slabs and the ambient mantle, could affect mantle flow and related surface observations significantly (e.g., Moresi & Gurnis, 1996; Tosi, Čadek, & Martinec, 2009; Zhong & Davies, 1999; Zhong et al., 2000; Čadek & Fleitout, 2003). However, such effects depend on buoyancy structure (Zhong & Davies, 1999) and are rather modest for the long-wavelength geoid at degrees 2 and 3 for seismically derived buoyancy (Ghosh et al., 2010; Moucha et al., 2007; Zhang & Christensen, 1993). While laboratory studies and some numerical models of subduction suggest that the slabs are strong with viscosity that could be 10^4–10^6 times stronger than the ambient mantle due to temperature-dependent viscosity (e.g., Billen & Hirth, 2007; Stadler et al., 2010), most geoid modeling studies suggest that the slabs are no more than 100 times stronger than the ambient mantle (Billen et al., 2003; Moresi & Gurnis, 1996; Yang & Gurnis, 2016; Zhong & Davies, 1999). Specifically, strong slabs could result in large surface topography and negative geoid anomalies over subduction zones that are inconsistent with the observation (Moresi & Gurnis, 1996; Zhong & Davies, 1999). However, using an idealized model of a subducted slab, Hines and Billen (2012) proposed that if the bending zone (i.e., outer rise and trench regions) of subducting lithosphere is weakened due to yielding, the geoid becomes insensitive to the slab strength.

Our models also show that slab strength strongly affects slab morphology and the geoid. Weaker slabs result in less coherent and more dispersed structures and are easier to penetrate through the 670 km phase transition (Figures S6a–S6h). Cases E1 and E2 with the weakest slab and Case E3 with the strongest slab both show significantly lower correlations to the observed geoid than that of Case B5 with moderately strong slab (Figure 6e). Therefore, our preferred slab viscosity is ~10–100 times larger than the ambient mantle and is consistent with previous geoid studies (Ghosh et al., 2010; Moresi & Gurnis, 1996; Yang & Gurnis, 2016; Zhong & Davies, 1999). The moderately strong slab could result from the combining effects of strong temperature-dependent viscosity (e.g., Billen & Hirth, 2007) and other weakening mechanisms, such as grain size reduction (e.g., Karato, 2008; Solomatov & Reese, 2008) and plastic yielding (Hines & Billen, 2012). It is important to point out that our models show significant sensitivity of the subduction zone geoid (i.e., degrees 4 to 12) to slab viscosity, although our models with 200-km wide weak plate margins effectively reduce bending strength of lithosphere. This result is different from Hines and Billen (2012), suggesting the importance in modeling the observed geoid with suitable wavelengths and configuration of subducted slabs as in our current study.

Our geoid models do not generate sufficiently large amplitudes for degrees 2 and 3 geoid anomalies compared with the observed ones, although they produce good geoid fits in subduction zones for degrees 4–12 (Figures 3, 5, and S7 for Cases A1 and B5). Since the insulating CMB boundary conditions in our models exclude upwelling thermal structures which are likely more important near the bottom part of the lower mantle (e.g., Leng & Zhong, 2008; MZ19), our models may underestimate the lower mantle structure that affects primarily the degrees 2 and 3 geoid (Hager & Richards, 1989). We showed that replacing the buoyancy structure below 1,500 km depth in our models with seismic structure could significantly improve the degrees 2 and 3 geoid fits, while having no significant effect on the geoid at degrees 4–12 (Figures 5a) and 5b. However, if the LLSVPs are compositionally distinct from and intrinsically denser than the background lower mantle (e.g., Davaille, 1999; McNamara, 2019; McNamara & Zhong, 2005), it is possible that the

thermal and chemical buoyancy in the bottom hundreds of kilometers of the mantle would be offset by each other, thus not contributing to the geoid at the surface (Liu & Zhong 2015, 2016).

The viscosity reduction due to Pv-pPv phase transition may decouple the slabs from the CMB, thus affecting the geoid amplitude significantly (e.g., Tosi, Čadek, & Martinec, 2009; Tosi, Čadek, Martinec, Yuen, et al., 2009; Ghosh et al., 2010; Wang et al., 2019). To test this effect, we recomputed Case B5 by reducing the viscosity by a factor of 15 either for the entire D″ layer (i.e., globally for the bottom 300 km of the mantle; Case B5e) or only for the cold slabs in the D″ layer (Hernlund et al., 2005; Case B5f). While the geoid at degrees 4–12 remains largely unchanged, the geoid amplitude at degrees 2–3 increases significantly and becomes comparable with the observed one due to the viscosity reduction of the D″ layer (Figures 5d, 3g, and 3h). We did not attempt to fine-tune D″ layer or pPv viscosity to fit degrees 2–3 geoid, given that our primary goal is to use the observed subduction zone geoid (i.e., degrees 4–12) to constrain the mantle viscosity. Interestingly, the increased geoid at degrees 2–3 for these two test calculations is accompanied with increased surface dynamic topography at degrees 2–3 (Figure 8f) which is now at ∼0.7–1.0 km, similar to predictions from previous modeling studies (e.g., Flament et al., 2013; Hager & Richards, 1989; Yang & Gurnis, 2016) and inferred from the observations (e.g., Davies et al., 2019). Liu and Zhong (2016) explained the necessity of ∼1 km dynamic topography at degree 2 for reproducing the observed ∼100 m degree-2 geoid as a consequence of the averaged ratio of geoid to dynamic topography kernels at ∼0.1 for degree 2 for most geoid models.

4.4. Potential Drawback and Future Directions

Our studies represent the first comprehensive effort in explaining the observed present-day subduction zone geoid and plate motion, using mantle buoyancy that is self-consistently generated from mantle convection models with plate motion history, but they have a number of drawbacks that can be improved in future studies. The first is about the lower mantle buoyancy that is associated with degrees 2–3 geoid anomalies, as discussed in Section 4.3. This may include considering isothermal CMB boundary conditions that would lead to mantle plume structures in the lower mantle (MZ19). Future studies may also consider long duration of plate motion history that affects the lower mantle structure (MZ19), although the uncertainties of more ancient plate motion history are large (e.g., Seton et al., 2012). Additionally, it remains a subject of debate whether the LLSVPs are of purely thermal or thermochemical origin (e.g., Davaille & Romanowicz, 2020; Davies, 2012; Ni et al., 2002; He & Wen, 2012; Schuberth et al., 2009), and this may have important implications for degrees 2 and 3 geoid (Liu & Zhong, 2015, 2016). The second is on considering additional mantle and lithospheric viscosity features, including non-Newtonian viscosity (e.g., Hines & Billen, 2012) and depth-variations in viscosity for the lower mantle (e.g., Mitrovica & Forte, 2004; Rudolph et al., 2015; Steinberger & Calderwood, 2006), although the viscosity increase at 1,000 km depth proposed by Rudolph et al. (2015) has been debated (e.g., Ghosh et al., 2017; Wang & Li, 2020; Yang & Gurnis, 2016). In particular, the implications of non-Newtonian rheology for non-uniform plate margin viscosity and lithospheric net rotation need to be further explored.

5. Conclusions

In this study, we formulate 3-D spherical mantle convection models with plate motion history and for the first time compute the geoid using the dynamically generated buoyancy to constrain the mantle viscosity. Our dynamic models employ depth- and temperature-dependent viscosities. Our models generate self-consistent present-day mantle thermal and buoyancy structures that are similar to the seismically observed slab structures and enable us to use the observed intermediate-wavelengths geoid and plate motions to place constraints on lithospheric and mantle viscosity. The main results are summarized as follows:

(1) Our convection models reproduce the primary slab structures observed in seismic models including stagnant slabs in the mantle transition zone in the western Pacific and other subduction zones. A thin weak layer below the 670-km phase change on a regional scale in subduction zones, not necessarily globally as in Mao and Zhong (2018), is sufficiently effective in producing the stagnant slabs

(2) Lithospheric viscosity including strong plate interiors and weak plate margins has significant effects on the geoid and surface plate motions. In particular, non-uniform viscosity of plate margins with weaker plate margins around the Pacific plate could effectively reproduce the observed plate motions including the net rotation of lithosphere and lead to better geoid fit

(3) In the preferred model as constrained by observations of slab structures and the subduction zone geoid (degrees 4–12), the lower mantle viscosity is $\sim$1.3–2.5 $\times$ 10^{22} Pa·s and is $\sim$30 and $\sim$600–1,000 times higher than that in the transition zone and asthenosphere, respectively. Our models prefer a weak asthenosphere but not a weak mantle transition zone, and also favor moderately strong slabs that are $\sim$10–100 times stronger than the ambient mantle. While the geoid at degrees 4–12 is mainly controlled by subducted slab structures in the top 1,500 km of the mantle that have developed since the Cretaceous, the degrees 2–3 geoid anomalies that are strongly related to deep lower mantle structures might be influenced by mantle convection further back in time

Data Availability Statement

Figures are drawn using the Generic Mapping Tools (GMT, www.soest.hawaii.edu/gmt/). The mantle convection code CitcomS is available at https://geodynamics.org/cig/software/citcoms/. All model input parameters are given in Tables 1 and 2, and all data are available at https://doi.org/10.6084/m9.figshare.13371140.v1.

References

Čadek, O., & Fleitout, L. (2003). Effect of lateral viscosity variations in the top 300 km on the geoid and dynamic topography. *Geophysical Journal International*, *152*(3), 566–580.

Becker, T. W. (2006). On the effect of temperature and strain-rate dependent viscosity on global mantle flow, net rotation, and plate-driving forces. *Geophysical Journal International*, *167*(2), 943–957. https://doi.org/10.1111/j.1365-246x.2006.03172.x

Becker, T. W. (2017). Superweak asthenosphere in light of upper mantle seismic anisotropy. *Geochem. Geophys. Geosyst.*, *18*(5), 1986–2003. https://doi.org/10.1002/2017gc006886

Becker, T. W., & Boschi, L. (2002). A comparison of tomographic and geodynamic mantle models. *Geochemistry, Geophysics, Geosystems*, *3*, a. https://doi.org/10.1029/2001GC000168

Bercovici, D. (2003). The generation of plate tectonics from mantle convection. *Earth and Planetary Science Letters*, *205*, 107–121. https://doi.org/10.1016/s0012-821x(02)01009-9

Bercovici, D., & Karato, S.-I. (2003). Whole-mantle convection and the transition-zone water filter. *Nature*, *425*, 39–44. https://doi.org/10.1038/nature01918

Billen, M. I., & Gurnis, M. (2001). A low viscosity wedge in subduction zones. *Earth and Planetary Science Letters*, *193*(1–2), 227–236. https://doi.org/10.1016/s0012-821x(01)00482-4

Billen, M. I., Gurnis, M., & Simons, M. (2003). Multiscale dynamics of the Tonga-Kermadec subduction zone. *Geophysical Journal International*, *153*, 359–388. https://doi.org/10.1046/j.1365-246x.2003.01915.x

Billen, M. I., & Hirth, G. (2007). Rheologic controls on slab dynamics. *Geochemistry, Geophysics, Geosystems*, *8*, a. Q08012. https://doi.org/10.1029/2007GC001597

Bower, D. J., Gurnis, M., & Seton, M. (2013). Lower mantle structure from paleogeographically constrained dynamic Earth models. *Geochemistry, Geophysics, Geosystems*, *14*(1), 44–63. https://doi.org/10.1029/2012gc004267

Bunge, H., Richards, M. A., Lithgow-Bertelloni, C., Baumgardner, J. R., Grand, S. P., & Romanowicz, B. A. (1998). Time scales and heterogeneous structure in geodynamic Earth models. *Science*, *280*(5360), 91–95. https://doi.org/10.1126/science.280.5360.91

Christensen, U. R. (1996). The influence of trench migration on slab penetration into the lower mantle. *Earth and Planetary Science Letters*, *140*(1–4), 27–39. https://doi.org/10.1016/0012-821x(96)00023-4

Christensen, U. R., & Yuen, D. A. (1985). Layered convection induced by phase transitions. *Journal of Geophysical Research*, *90*(B12), 10291–10300. https://doi.org/10.1029/jb090ib12p10291

Conrad, C. P., & Lithgow-Bertelloni, C. (2002). How mantle slabs drive plate tectonics. *Science*, *298*(5591), 207–209. https://doi.org/10.1126/science.1074161

Davaille, A. (1999). Simultaneous generation of hotspots and superswells by convection in a heterogeneous planetary mantle. *Nature*, *402*(6763), 756. https://doi.org/10.1038/45461

Davaille, A., & Romanowicz, B. (2020). Deflating the LLSVPs: Bundles of Mantle Thermochemical Plumes Rather Than Thick Stagnant "Piles". *Tectonics*, *39*(10), e2020TC006265. https://doi.org/10.1029/2020tc006265

Davies, D. R., Goes, S., Davies, J. H., Schuberth, B. S. A., Bunge, H.-P., & Ritsema, J. (2012). Reconciling dynamic and seismic models of Earth's lower mantle: The dominant role of thermal heterogeneity. *Earth and Planetary Science Letters*, *353–354*, 253–269. https://doi.org/10.1016/j.epsl.2012.08.016

Davies, D. R., Valentine, A. P., Kramer, S. C., Rawlinson, N., Hoggard, M. J., Eakin, C. M., & Wilson, C. R. (2019). Earth's multi-scale topographic response to global mantle flow. *Nature Geoscience*, *12*(10), 845–850. https://doi.org/10.1038/s41561-019-0441-4

Davies, G. F. (1988). Role of the lithosphere in mantle convection. *Journal of Geophysical Research*, *93*(B9), 10451–10466. https://doi.org/10.1029/jb093ib09p10451

Fei, Y., Van Orman, J., Li, J., van Westrenen, W., Sanloup, C., Minarik, W., et al. (2004). Experimentally determined postspinel transformation boundary in Mg2SiO4 using MgO as an internal pressure standard and its geophysical implications. *Journal of Geophysical Research*, *109*, B02305. https://doi.org/10.1029/2003jb002562

Flament, N., Gurnis, M., & Müller, R. D. (2013). A review of observations and models of dynamic topography. *Lithosphere*, *5*(2), 189–210. https://doi.org/10.1130/l245.1

French, S. W., & Romanowicz, B. (2015). Broad plumes rooted at the base of the Earth's mantle beneath major hotspots. *Nature*, *525*(7567), 95. https://doi.org/10.1038/nature14876

French, S. W., & Romanowicz, B. A. (2014). Whole-mantle radially anisotropic shear velocity structure from spectral-element waveform tomography. *Geophysical Journal International*, *199*(3), 1303–1327. https://doi.org/10.1093/gji/ggu334

Fukao, Y., & Obayashi, M. (2013). Subducted slabs stagnant above, penetrating through, and trapped below the 660 km discontinuity. *Journal of Geophysical Research: Solid Earth*, *118*(11), 5920–5938. https://doi.org/10.1002/2013jb010466

Gérault, M., Becker, T. W., Kaus, B. J. P., Faccenna, C., Moresi, L., & Husson, L. (2012). The role of slabs and oceanic plate geometry in the net rotation of the lithosphere, trench motions, and slab return flow. *Geochemistry, Geophysics, Geosystems*, *13*, a. Q04001. https://doi.org/10.1029/2011GC003934

Ghosh, A., Becker, T. W., & Zhong, S. J. (2010). Effects of lateral viscosity variations on the geoid. *Geophysical Research Letters*, *37*, a. L01301. https://doi.org/10.1029/2009GL040426

Ghosh, A., & Holt, W. E. (2012). Plate motions and stresses from global dynamic models. *Science*, *335*(6070), 838–843. https://doi.org/10.1126/science.1214209

Ghosh, A., Holt, W. E., & Wen, L. (2013). Predicting the lithospheric stress field and plate motions by joint modeling of lithosphere and mantle dynamics. *Journal of Geophysical Research: Solid Earth*, *118*(1), 346–368. https://doi.org/10.1029/2012jb009516

Ghosh, A., Thyagarajulu, G., & Steinberger, B. (2017). The importance of upper mantle heterogeneity in generating the Indian Ocean geoid low. *Geophysical Research Letters*, *44*(19), 9707–9715. https://doi.org/10.1002/2017gl075392

Gripp, A. E., & Gordon, R. G. (2002). Young tracks of hotspots and current plate velocities. *Geophysical Journal International*, *150*(2), 321–361. https://doi.org/10.1046/j.1365-246x.2002.01627.x

Hager, B. H. (1984). Subducted slabs and the geoid: Constraints on mantle rheology and flow. *Journal of Geophysical Research*, *89*(B7), 6003–6015. https://doi.org/10.1029/jb089ib07p06003

Hager, B. H., Clayton, R. W., Richards, M. A., Comer, R. P., & Dziewonski, A. M. (1985). Lower mantle heterogeneity, dynamic topography and the geoid. *Nature*, *313*(6003), 541. https://doi.org/10.1038/313541a0

Hager, B. H., & Richards, M. A. (1989). Long-wavelength variations in Earth's geoid: Physical models and dynamical implications. *Philosophical Transactions of the Royal Society A*, *328*(1599), 309–327.

Hernlund, J. W., Thomas, C., & Tackley, P. J. (2005). A doubling of the post-perovskite phase boundary and structure of the Earth's lowermost mantle. *Nature*, *434*(7035), 882–886. https://doi.org/10.1038/nature03472

He, Y., & Wen, L. (2012). Geographic boundary of the "Pacific Anomaly" and its geometry and transitional structure in the north. *Journal of Geophysical Research*, *117*, B09308. https://doi.org/10.1029/2012JB009436

Hines, J. M., & Billen, M. I. (2012). Sensitivity of the short- to intermediate-wavelength geoid to rheologic structure in subduction zones. *Journal of Geophysical Research*, *117*, a. https://doi.org/10.1029/2011JB008978

Huang, J., & Zhong, S. (2005). Sublithospheric small-scale convection and its implications for the residual topography at old ocean basins and the plate model. *Journal of Geophysical Research*, *110*, B05404. https://doi.org/10.1029/2004JB003153

Karato, S.-I. (2008). *Deformation of earth materials: An introduction to the rheology of solid earth*. Cambridge University Press.

Karato, S.-I., & Karki, B. B. (2001). Origin of lateral variation of seismic wave velocities and density in the deep mantle. *Journal of Geophysical Research*, *106*(B10), 21771–21783. https://doi.org/10.1029/2001jb000214

King, S. D. (1995). Radial models of mantle viscosity: Results from a genetic algorithm. *Geophysical Journal International*, *122*(3), 725–734. https://doi.org/10.1111/j.1365-246x.1995.tb06831.x

King, S. D. (2002). Geoid and topography over subduction zones: The effect of phase transformations. *Journal of Geophysical Research*, *107*(B1), 2. https://doi.org/10.1029/2000JB000141

King, S. D., Gable, C. W., & Weinstein, S. A. (1992). Models of convection-driven tectonic plates: A comparison of methods and results. *Geophysical Journal International*, *109*(3), 481–487. https://doi.org/10.1111/j.1365-246x.1992.tb00111.x

Kreemer, C., Holt, W. E., & Haines, A. J. (2003). An integrated global model of present-day plate motions and plate boundary deformation. *Geophysical Journal International*, *154*(1), 8–34. https://doi.org/10.1046/j.1365-246x.2003.01917.x

Lee, C. K., Han, S. C., & Steinberger, B. (2011). Influence of variable uncertainties in seismic tomography models on constraining mantle viscosity from geoid observations. *Physics of the Earth and Planetary Interiors*, *184*(1–2), 51–62. https://doi.org/10.1016/j.pepi.2010.10.012. https://doi.org/10.1016/j.pepi.2010.10.012

Leng, W., & Zhong, S. (2008). Controls on plume heat flux and plume excess temperature. *Journal of Geophysical Research*, *113*, B04408. https://doi.org/10.1029/2007JB005155

Litasov, K. D., Ohtani, E., Sano, A., Suzuki, A., & Funakoshi, K. (2005). Wet subduction versus cold subduction. *Geophysical Research Letters*, *32*, L13312. https://doi.org/10.1029/2005GL022921

Lithgow-Bertelloni, C., & Richards, M. A. (1998). The dynamics of Cenozoic and Mesozoic plate motions. *Reviews of Geophysics*, *36*(1), 27–78. https://doi.org/10.1029/97rg02282

Liu, X., & Zhong, S. (2015). The long-wavelength geoid from three-dimensional spherical models of thermal and thermochemical mantle convection. *Journal of Geophysical Research: Solid Earth*, *120*(6), 4572–4596. https://doi.org/10.1002/2015jb012016

Liu, X., & Zhong, S. (2016). Constraining mantle viscosity structure for a thermochemical mantle using the geoid observation. *Geochemistry, Geophysics, Geosystems*, *17*(3), 895–913. https://doi.org/10.1002/2015gc006161

Müller, R. D., Dutkiewicz, A., Seton, M., & Gaina, C. (2013). Seawater chemistry driven by supercontinent assembly, breakup, and dispersal. *Geology*, *41*(8), 907–910. https://doi.org/10.1130/g34405.1

Mao, W., & Zhong, S. (2018). Slab stagnation due to a reduced viscosity layer beneath the mantle transition zone. *Nature Geoscience*, *11*(11), 876–881. https://doi.org/10.1038/s41561-018-0225-2

Mao, W., & Zhong, S. (2019). Controls on global mantle convective structures and their comparison with seismic models. *Journal of Geophysical Research: Solid Earth*, *124*(8), 9345–9372. https://doi.org/10.1029/2019jb017918

McNamara, A. K. (2019). A review of large low shear velocity provinces and ultra low velocity zones. *Tectonophysics*, *760*, 199–220. https://doi.org/10.1016/j.tecto.2018.04.015

McNamara, A. K., & Zhong, S. (2005). Thermochemical structures beneath Africa and the Pacific Ocean. *Nature*, *437*(7062), 1136. https://doi.org/10.1038/nature04066

Mitrovica, J. X., & Forte, A. M. (2004). A new inference of mantle viscosity based upon joint inversion of convection and glacial isostatic adjustment data. *Earth and Planetary Science Letters*, *225*(1–2), 177–189. https://doi.org/10.1016/j.epsl.2004.06.005

Molnar, P., England, P. C., & Jones, C. H. (2015). Mantle dynamics, isostasy, and the support of high terrain. *Journal of Geophysical Research: Solid Earth*, *120*(3), 1932–1957. https://doi.org/10.1002/2014jb011724

Moresi, L., & Gurnis, M. (1996). Constraints on the lateral strength of slabs from three-dimensional dynamic flow models. *Earth and Planetary Science Letters*, *138*(1–4), 15–28. https://doi.org/10.1016/0012-821x(95)00221-w

Morgan, W. J. (1965). Gravity anomalies and convection currents: 1. A sphere and cylinder sinking beneath the surface of a viscous fluid. *Journal of Geophysical Research*, *70*(24), 6175–6187. https://doi.org/10.1029/jz070i024p06175

Moucha, R., Forte, A. M., Mitrovica, J. X., & Daradich, A. (2007). Lateral variations in mantle rheology: Implications for convection related surface observables and inferred viscosity models. *Geophysical Journal International*, *169*(1), 113–135. https://doi.org/10.1111/j.1365-246x.2006.03225.x

Nestola, F., & Smyth, J. R. (2015). Diamonds and water in the deep Earth: A new scenario. *International Geology Review*, *58*(3), 263–276. https://doi.org/10.1080/00206814.2015.1056758

Ni, S., Tan, E., Gurnis, M., & Helmberger, D. (2002). Sharp sides to the African superplume. *Science*, *296*(5574), 1850–1852. https://doi.org/10.1126/science.1070698

O'Neill, C., Müller, D., & Steinberger, B. (2005). On the uncertainties in hot spot reconstructions and the significance of moving hot spot reference frames. *Geochemistry, Geophysics, Geosystems*, *6*, a. Q04003. https://doi.org/10.1029/2004GC000784

Panasyuk, S. V., & Hager, B. H. (1998). A model of transformational superplasticity in the upper mantle. *Geophysical Journal International*, *133*(3), 741–755. https://doi.org/10.1046/j.1365-246x.1998.00539.x

Peltier, W. R. (1998). Postglacial variations in the level of the sea: Implications for climate dynamics and solid-earth geophysics. *Reviews of Geophysics*, *36*(4), 603–689. https://doi.org/10.1029/98rg02638

Pollitz, F. F., Wicks, C., & Thatcher, W. (2001). Mantle flow beneath a continental strike-slip fault: Postseismic deformation after the 1999 Hector Mine earthquake. *Science*, *293*, 1814–1818. https://doi.org/10.1126/science.1061361

Ricard, Y., Richards, M., Lithgow-Bertelloni, C., & Le Stunff, Y. (1993). A geodynamic model of mantle density heterogeneity. *Journal of Geophysical Research*, *98*(B12), 21895–21909. https://doi.org/10.1029/93jb02216

Richards, M. A., & Lenardic, A. (2018). The Cathles parameter (Ct): A geodynamic definition of the asthenosphere and implications for the nature of plate tectonics. *Geochemistry, Geophysics, Geosystems*, *19*(12), 4858–4875.

Ritsema, J., Deuss, A., Van Heijst, H. J., & Woodhouse, J. H. (2011). S40RTS: A degree-40 shear-velocity model for the mantle from new Rayleigh wave dispersion, teleseismic traveltime and normal-mode splitting function measurements. *Geophysical Journal International*, *184*(3), 1223–1236. https://doi.org/10.1111/j.1365-246x.2010.04884.x

Rudolph, M. L., Leki, V., & Lithgow-Bertelloni, C. (2015). Viscosity jump in Earths mid-mantle. *Science*, *350*(6266), 1349–1352. https://doi.org/10.1126/science.aad1929

Rudolph, M. L., & Zhong, S. J. (2014). History and dynamics of net rotation of the mantle and lithosphere. *Geochemistry, Geophysics, Geosystems*, *15*(9), 3645–3657. https://doi.org/10.1002/2014gc005457

Schuberth, B. S. A., Bunge, H.-P., & Ritsema, J. (2009). Tomographic filtering of high-resolution mantle circulation models: Can seismic heterogeneity be explained by temperature alone? *Geochemistry, Geophysics, Geosystems*, *10*(5), a. Q05W03. https://doi.org/10.1029/2009GC002401

Semple, A. G., & Lenardic, A. (2020). Feedbacks between a non-newtonian upper mantle, mantle viscosity structure, and mantle dynamics. *Geophysical Journal International*, *224*(2), 961–972.ggaa495. https://doi.org/10.1093/gji/ggaa495

Seton, M., Müller, R. D., Zahirovic, S., Gaina, C., Torsvik, T., Shephard, G., & Chandler, M. (2012). Global continental and ocean basin reconstructions since 200 Ma. *Earth-Science Reviews*, *113*(3–4), 212–270. https://doi.org/10.1016/j.earscirev.2012.03.002

Simmons, N. A., Forte, A. M., & Grand, S. P. (2009). Joint seismic, geodynamic and mineral physical constraints on three-dimensional mantle heterogeneity: Implications for the relative importance of thermal versus compositional heterogeneity. *Geophysical Journal International*, *177*(3), 1284–1304. https://doi.org/10.1111/j.1365-246x.2009.04133.x

Solomatov, V. S., & Reese, C. C. (2008). Grain size variations in the Earth's mantle and the evolution of primordial chemical heterogeneities. *Journal of Geophysical Research*, *113*, B07408. https://doi.org/10.1029/2007JB005319

Spasojevic, S., Gurnis, M., & Sutherland, R. (2010). Mantle upwellings above slab graveyards linked to the global geoid lows. *Nature Geoscience*, *3*(6), 435–438. https://doi.org/10.1038/ngeo855

Stadler, G., Gurnis, M., Burstedde, C., Wilcox, L. C., Alisic, L., & Ghattas, O. (2010). The dynamics of plate tectonics and mantle flow: From local to global scales. *Science*, *329*(5995), 1033–1038. https://doi.org/10.1126/science.1191223

Steinberger, B., & Calderwood, A. R. (2006). Models of large-scale viscous flow in the Earth's mantle with constraints from mineral physics and surface observations. *Geophysical Journal International*, *167*(3), 1461–1481. https://doi.org/10.1111/j.1365-246x.2006.03131.x

Steinberger, B., Torsvik, T. H., & Becker, T. W. (2012). Subduction to the lower mantle - a comparison between geodynamic and tomographic models. *Solid Earth*, *3*(2), 415. https://doi.org/10.5194/se-3-415-2012

Stixrude, L., & Lithgow-Bertelloni, C. (2005). Thermodynamics of mantle minerals - I. Physical properties. *Geophysical Journal International*, *162*(2), 610–632. https://doi.org/10.1111/j.1365-246x.2005.02642.x

Stixrude, L., & Lithgow-Bertelloni, C. (2011). Thermodynamics of mantle minerals - II. Phase equilibria. *Geophysical Journal International*, *184*(3), 1180–1213. https://doi.org/10.1111/j.1365-246x.2010.04890.x

Tosi, N., Čadek, O., & Martinec, Z. (2009). Subducted slabs and lateral viscosity variations: Effects on the long-wavelength geoid. *Geophysical Journal International*, *179*(2), 813–826. https://doi.org/10.1111/j.1365-246x.2009.04335.x

Tosi, N., Čadek, O., Martinec, Z., Yuen, D. A., & Kaufmann, G. (2009). Is the long-wavelength geoid sensitive to the presence of postperovskite above the core-mantle boundary? *Geophysical Research Letters*, *36*(5). https://doi.org/10.1029/2008gl036902

Turcotte, D. L., & Schubert, G. (2014). *Geodynamics* (3rd ed.) (pp. 192–193). Cambridge University Press.

Wang, X., Holt, W. E., & Ghosh, A. (2019). Joint modeling of lithosphere and mantle dynamics: Sensitivity to viscosities within the lithosphere, asthenosphere, transition zone, and D″ layers. *Physics of the Earth and Planetary Interiors*, *293*, 106263. https://doi.org/10.1016/j.pepi.2019.05.006

Wang, Y., & Li, M. (2020). Constraining mantle viscosity structure from a statistical analysis of slab stagnation events. *Geochemistry, Geophysics, Geosystems*, *21*, e2020GC009286. https://doi.org/10.1029/2020GC009286

Williams, Q., & Hemley, R. J. (2001). Hydrogen in the deep earth. *Annual Review of Earth and Planetary Sciences*, *29*, 365–418. https://doi.org/10.1146/annurev.earth.29.1.365

Yang, T., & Gurnis, M. (2016). Dynamic topography, gravity and the role of lateral viscosity variations from inversion of global mantle flow. *Geophysical Journal International*, *207*(2), 1186–1202. https://doi.org/10.1093/gji/ggw335

Zhang, N., Zhong, S., & Flowers, R. M. (2012). Predicting and testing continental vertical motion histories since the Paleozoic. *Earth and Planetary Science Letters*, *317–318*, 426–435. https://doi.org/10.1016/j.epsl.2011.10.041

Zhang, N., Zhong, S., Leng, W., & Li, Z.-X. (2010). A model for the evolution of the Earth's mantle structure since the Early Paleozoic. *Journal of Geophysical Research*, *115*, B06401. https://doi.org/10.1029/2009JB006896

Zhang, S., & Christensen, U. (1993). Some effects of lateral viscosity variations on geoid and surface velocities induced by density anomalies in the mantle. *Geophysical Journal International*, *114*(3), 531–547. https://doi.org/10.1111/j.1365-246x.1993.tb06985.x

Zhong, S. (2001). Role of ocean-continent contrast and continental keels on plate motion, net rotation of lithosphere, and the geoid. *Journal of Geophysical Research*, *106*(B1), 703–712. https://doi.org/10.1029/2000jb900364

Zhong, S., & Davies, G. F. (1999). Effects of plate and slab viscosities on the geoid. *Earth and Planetary Science Letters*, *170*(4), 487–496. https://doi.org/10.1016/s0012-821x(99)00124-7

Zhong, S., & Gurnis, M. (1994). Role of plates and temperature-dependent viscosity in phase change dynamics. *Journal of Geophysical Research*, *99*(B8), 15903–15917. https://doi.org/10.1029/94jb00545

Zhong, S., & Gurnis, M. (1995). Mantle convection with plates and mobile, faulted plate margins. *Science*, *267*(5199), 838–843. https://doi.org/10.1126/science.267.5199.838

Zhong, S., & Gurnis, M. (1996). Interaction of weak faults and non-Newtonian rheology produces plate tectonics in a 3D model of mantle flow. *Nature*, *383*(6597), 245–247. https://doi.org/10.1038/383245a0

Zhong, S., McNamara, A., Tan, E., Moresi, L., & Gurnis, M. (2008). A benchmark study on mantle convection in a 3-D spherical shell using CitcomS. *Geochemistry, Geophysics, Geosystems*, *9*, a. Q10017. https://doi.org/10.1029/2008GC002048

Zhong, S., Zuber, M. T., Moresi, L., & Gurnis, M. (2000). Role of temperature-dependent viscosity and surface plates in spherical shell models of mantle convection. *Journal of Geophysical Research*, *105*(B5), 11063–11082. https://doi.org/10.1029/2000jb900003